Fabrication and Model Based Position Estimation of Novel Laser Processed Shape Memory Alloy Actuator with an Embedded Strain Gauge Sensor

by

Nima Zamani

A thesis
presented to the University of Waterloo
in fulfillment of the
thesis requirement for the degree of
Master of Applied Science
in
Mechanical and Mechatronics Engineering

Waterloo, Ontario, Canada, 2017

I hereby declare that I am the sole author of this thesis. This is a true copy of the thesis, including any required final revisions, as accepted by my examiners.

I understand that my thesis may be made electronically available to the public.

Abstract

Shape Memory Alloys have sparked great amount of interest in the field of actuation over the past decades. Until now, sensorless position estimation of SMA actuators under dynamic unknown applied stresses has not been feasible due to the complexity of the system and the number of unknown parameters which the proposed extra information obtained from the embedded sensor solves. In this thesis, a novel laser processed NiTi Shape Memory Alloy (SMA) actuator is proposed containing two different material compositions in one monolithic piece of actuator wire. Each of these compositions behaves differently at room temperature, one exhibits a shape memory effect (SME) for actuation, and the other is pseudo-elastic (PE) which is used to enable an embedded sensor. Fabrication of the wire included laser processing, heat-treatment, and cold-working procedures. The actuator wire was subsequently trained to stabilize its properties using iso-stress thermal cycling. Additionally, a novel model-based sensorless position estimation algorithm is presented. Proposed model can estimate the position of the actuator under varying applied stresses with an approximate accuracy of 95% only using dual resistance measurements across the two different material compositions. The proposed actuator has significant application in robotics, wearables, haptics, automotive, and any other application which the mechanical load is not known in advance. Two simple position and force controller schemes using the proposed dual-resistance measurement position (and force) estimation are discussed and the control results presented. The proposed position estimation algorithm is used for the feedback-signal of a simple PID position and force controller scheme. Moreover, another novel sensorless position estimation of SMA actuator wires are presented using the power measurement of the standing wave cause by the reflection of a high-frequency signal at an un-terminated end.

Acknowledgements

I would like to sincerely thank my supervisor, Prof. Behrad Khamesee, for his support and guidance during my studies. I'm grateful for the time and effort he put during this project.

I would like to thank SmarterAlloys Inc., specifically Dr. Mohammad Ibraheem Khan, for providing resources and guidance for me to complete my studies successfully. I appreciate Prof. Norman Zhou and the Centre for Advanced Materials Joining (CAMJ) for providing some of the necessary equipment for fabricating the SMA actuator wire.

This work has been supported by the Natural Sciences and Engineering Research Council of Canada (NSERC) Industrial Partnership Program.

To My Amazing Family

Table of Contents

List of Tables

List of Figures

Chapter 1

Introduction

Shape Memory Alloys (SMAs) are an extraordinary class of materials which exhibit unique properties including Shape Memory Effect (SME) and Pseudo-Elasticity (PE). The first observation of SME behavior occurred in 1932 by Arne Olander [1] with Cadmium-Gold alloy. However, it was not until the 1960s which the term Shape Memory Alloys were given to a set of materials which exhibit similar properties. Numerous alloy compositions of shape memory alloys have been identified, including CuAlNi, TiNb and FePt. However the most widely used and commercially available SMA is NiTi, commonly referred to as Nitinol. NiTi poses several advantages over other actuators such as high force to mass ratio, large recoverable strain, super-elasticity, and bio-compatibility.

Over the past decades, there have been significant advances in both understanding the behavior of existing SMA's and discovering new compositions. This has enabled the significant use of these alloys in a variety of applications, such as bio-medical vascular stents, automotive, robotics, aviation, and vibration absorption to name a few. However, there still remains two major drawbacks that severely limit the application of SMA's, including the actuation speed and sensor-less controllability under varying loading conditions. There are several ways of dealing with the actuation speed limitation of SMA such as using an

active cooling device [2], increasing the surface are to volume ratio using a bundle of wires instead of a single thicker one [3, 4, 5], or using high temperature SMAs such as the most common high temperature SMAs NiTiHf & NiTiXr [6, 7]. However, the second limitation is substantially more difficult to overcome using existing methods.

1.1 Motivation

Based on previous literature, position control of SMA actuators dates back decades, and many different control techniques have been implemented using different feedback signals. The most reliable and commonly used feedback signal is a direct position measurement [5, 8, 9, 10, 11, 12, 13]. However, position sensors can be expensive and add complexity to the actuator assembly; thus, preventing SMAs to compete with other actuation technologies such as piezoelectric and magnetic actuators. Sensor-less methods such as using Electrical Resistance (ER) as a feedback signal has also been used to control the position of the actuator [14, 15, 16]. However, in many of the studies, the applied stress is either constant or known in advance and has a monotonic relationship with displacement such as springs [16, 17, 18, 19, 8, 20, 15]. One of the first attempts at resistance feedback control was conducted by Ikuta in the late 1980s [14], and since then there have been many other studies seeking to control SMA actuators using ER feedback [21, 22, 23]. There are other sensorless methods such as inductance measurements of SMA springs and coils [24, 25, 26]. however, this method would not be useful for wire form due to a small change in the inductance of wires during shape change.

1.2 Objective and Scope

Using the Multiple-Memory-Material (MMM) technology & Laser Processing of SMAs to be able to locally alter their thermo-mechanical behaviour creates a in exploring the different ways The objective of this dissertation is to:

1. Design and make an automated wire feeding and laser processing SMA fabrication setup.

2. Explore the effects of laser pulse power and time on the thermo-mechanical properties of NiTi SMA wire.

3. Propose and validate an actuator design with an embedded strain gauge sensor which could be used in a sensorless fashion using dual-resistance measurements.

4. Design and fabricate the electronic circuitry required for the joules heating of the SMA actuation, dual-resistance measurements as well as other measurements needed for validation.

5. Propose and validate a position estimation algorithm based on the dual-resistance measurements that could be used in a control system to control the actuator position (or force) under dynamic and unknown stress levels.

6. Implement a simple PID controller which uses the dual-resistance measurement along with the position estimation algorithm in order to control the position of the proposed SMA actuator design.

7. Present other novel sensor-less position estimation methods.

1.3 Thesis Organization

This thesis is divided into eight major chapters; The first two chapters are introduction and literature review which contain background information regarding SMAs and the state of the SMA actuation at the current time. The third chapter discusses the fabrication process of the proposed actuator design as well as the setups and equipment used in the fabrication process. Additionally, it presents some of the effects of fabrication process parameters on the material properties.

The fourth chapter discusses the actuation experimental test setup which is used for both the position estimation and position control chapters. Additionally, this chapter presents some of the raw data gathered by the experimental setup. The fifth chapter is the most important and the heart of the thesis. It models both the PE and SME regions of the actuator. It discusses the use of the modelling in a sensor-less dual resistance position estimation algorithm as well.

The sixth chapter proposes another novel sensor-less position estimation method using high-frequency signal reflection power measurement. Chapter seven uses the proposed estimation algorithm in a PID feedback loop to control the position and force in a sensor-less fashion. Finally, Chapter eight concludes the thesis findings and offers future steps to bring this novel approach to SMA actuator design closer to industrial applications.

1.4 Novelty

In this thesis, there are three novel concepts. The first one is the idea of incorporating two different material properties in one monolithic actuator for sensing capabilities. The second concept is the use of power measurement of a reflected high-frequency signal to

estimated the length (position) of and SMA actuator. Finally, the third is the presented data showing the fine tuning capability of SMA phase transformation temperatures by changing the laser pulse power and pulse time.

Chapter 2

Literature Review

2.1 NiTi Shape Memory Alloy

NiTi SMAs exhibit two inherent properties: Pseudo-Elasticity (PE) and Shape Memory Effect (SME). Both PE and SME properties of SMA occur due to a reversible solid-state transformation between Austenite and Martensite phases. This transformation can be caused by a change in the temperature or the stress which SMA experiences. In fact temperature and stress, which are states of the material, act as opposing force concerning the causality of the phase transformation. Temperature-induced phase transformation which is observed more prominently in SME and Stress-induced phase transformation which is observed more prominently in PE are discussed in detail in sections 2.1.3 & 2.1.4 correspondingly. As shown in Figure 2.7, there are also situations where both stress and temperature play more of an even role in the phase transformation.

The lattice structure of the Austenite and Martensite phases of NiTi SMA is shown in Figure 2.1. Austenite has a B2 centric lattice while martensite has a B19. In fact, it is the volumetric change in the lattice formation that causes the significant recoverable shape change ability to SMAs. Typically, NiTi SMAs have a maximum recoverable strain

of approximately 10%. Like many alloys, NiTi SMAs have poly-crystalline microstructure. The final mechanical proprieties such as maximum amount of actuation and the stress-strain relationship for a given SMA actuator depends highly on the orientations of the phases inside the grains. Single crystalline NiTi SMAs are also produced with interesting properties; however, the production cost is very prohibitive.

Due to the unique properties of SMAs mentioned above, it is only logical for the thermal properties of SMAs to be very related to the mechanical properties as well. Therefore, a very common test performed on SMAs is Differential Scanning Calorimetry (DSC). DSC results provide many different thermal properties of SMAs such as transformations temperatures, and the heat capacity of the wire is a function temperature. Transformation temperatures are temperatures at which the solid phase Austenite to Martensite transformations occur. These self-explanatory temperatures are as follows: Martensite Start (M_s), Martensite Finish(M_f), Austenite Start(A_s), and Austenite Finish(A_f). A sample of a DSC result is shown in Figure 2.2 with the transformation temperatures labeled and the direction of transformation as well as heat are indicated.

2.1.1 NiTi Phase Diagram

As mentioned previously, one of the most common and used SMAs is NiTi. Thermo-mechanical properties of NiTi SMA is sensitive to its chemical composition. Even a relatively small change of 0.1 atomic% change in chemical composition can have approximately 10 $^{\circ}C$ change in the transformation temperatures [29]. Therefore, only a relatively narrow and very specific range of compositions of Nickel and Titanium give NiTi alloy with the desired properties. Figure 2.3 shows the Nickel-Titanium binary phase diagram system. NiTi is the only stable Intermetallic Compound known which exhibit shape memory properties. As shown in Figure 2.3, NiTi IMC is located between other IMCs such as Ti2Ni and

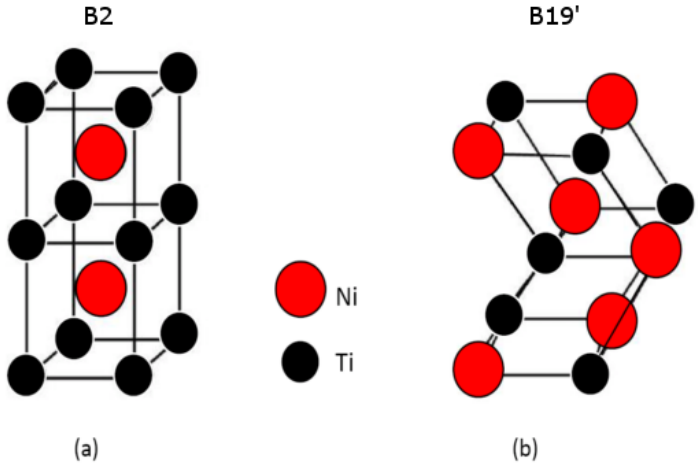

Figure 2.1: NiTi SMA Lattice Structure of B2 Austenite and B19' Martensite taken from [27] with modification.

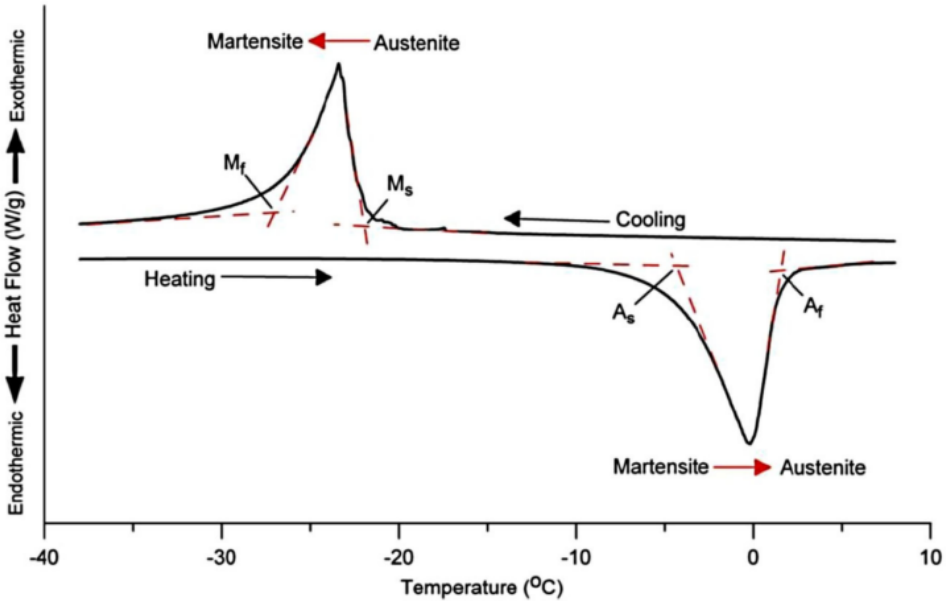

Figure 2.2: Sample of DSC results with M_s M_f A_s A_f transition temperatures labeled. [28]

TiNi3. These IMCs do not exhibit any shape memory properties and are mostly brittle in nature. These secondary IMCs typically exist in the form of precipitates in the NiTi IMC matrix. The existence and size of these secondary IMCs precipitates can have both desirable and undesirable effects. For example, Ti2Ni can form easily in Ti-rich alloy compositions, especially in the presence of Oxygen. Ti2Ni is very detrimental to the life and properties of NiTi SMAs and in most cases leads to breakages of material. Thus, this is crucial for processes such as welding and laser processing to properly shield the process regions which undergo high temperatures using a noble gas such as Argon. On the other hand, the existence of Ti3Ni4 is very beneficial to the stability of the structure of the NiTi poly-crystalline grains. These leads to better thermo-mechanical properties, shorter training times, and cycle life.

NiTi is a stoichiometric intermetallic at room temperature and for any solubility or diffusion to occur the temperature needs to exceed 650 degrees Celsius. Therefore, the material remains stable below 650 degrees Celsius in stress-free conditions. About 650 degrees Ni can get solutionized into NiTi to produce a more Ni-rich material. On the other hand aging heat-treatment at lower temperature can induce Ni-rich precipitates and case the matrix to be more Ti-rich. By various heat treatment techniques, such as the ones explained, thermal and mechanical properties of NiTi SMAs can be modified to suit an application. Even though heat treating SMAs such as NiTi is a very useful and crucial tool in modifying the thermal and mechanical properties of SMAs, it is mostly used on bulk material and obtaining a localized heat-treatment is very difficult without effecting the resit of the material due to thermal conduction.

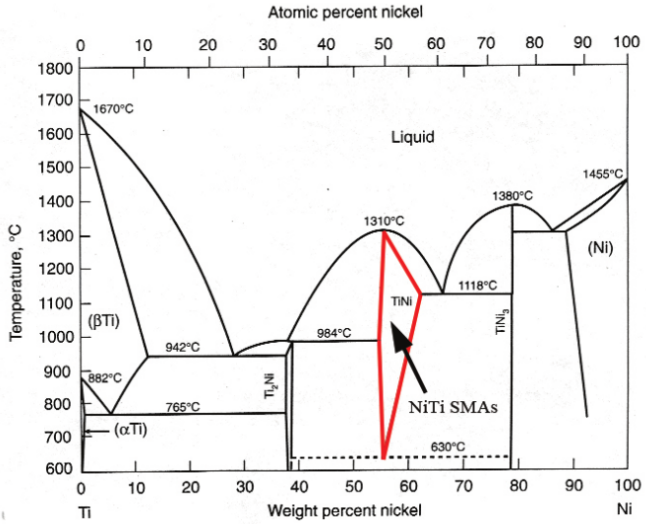

Figure 2.3: Binary Nickel-Titanium Phase Diagram with the NiTi alloy region indicated in red.. [30]

2.1.2 Ternary NiTiX & High-Temperature SMAs

As briefly discussed before, the simple binary NiTi SMA enjoys many advantages such as wide availability, ease of production, relatively low cost; however, it suffers from some serious deficiencies as well. One of these shortcomings is the large thermo-mechanical hysteresis of NiTi SMA. This large hysteresis is very problematic for control applications, and memory-based non-linear control schemes are needed to handle both the hysteresis and the non-linearity of the system. Te addition of a ternary species such as Copper to the conventional NiTi SMA has been shown to improve this shortcoming significantly. In addition to copper, other examples of ternary NiTi-based SMAs such as chromium, cobalt, manganese and iron have been shown to act as austenite stabilizers. However, these stabilizers decrease the transformation temperatures, and thus, reducing the frequency (speed) of the actuation. So utilizing these ternary elements should be done with caution.

On of the other major shortcoming of NiTi SMAs is the low actuation speed. This problem which exhibits itself mostly while the material is cooling is due to the relatively low transformation temperatures of NiTi. The Even highest temperature of NiTi has a A_f of approximately 90 degrees Celsius. By adding elements such as Zirconium, Hafnium, Palladium, Gold, Platinum and other heavier elements, the transformation temperature of the newly formed ternary SMA is significantly increase. This class of materials is referred to as High-Temperature SMAs (HTSMAs). This increase in transformation temperature causes the temperature difference between the material and the ambient to increase which in return increases the amount of convectional heat transfer from the SMA to the environment. In addition to improvements in speed, these SMA become available for some applications which operate at high temperatures which could not take advantage on the regular NiTi.

2.1.3 Temperature Induced Phase Transformation & Shape Memory Effect

The most well know behaviour of SMAs for actuation purposes is the Shape Memory Effect (SME) effect of the SMA. SME is the ability of the material to remember it's cold-forge shape and revert to it from a deformed shape upon heating. This cycle is summarized in Figure 2.4 a & b. As mentioned before in section 2.1, the process of SME occurs due to temperature-induced solid-state phase transformation between Austenite and Martensite phases. Austenite is the high-temperature phase, and Martensite is the low-temperature phase. For a regular one-way SME, the deformation of the original shape is necessary for any actuation to occur. The deformation takes the material from twinned Martensite to de-twinned Martensite as shown by Figure 2.4 a. Upon heating the material transforms back to the rigid Austenite phase. When the material is cooling, it transforms back to the

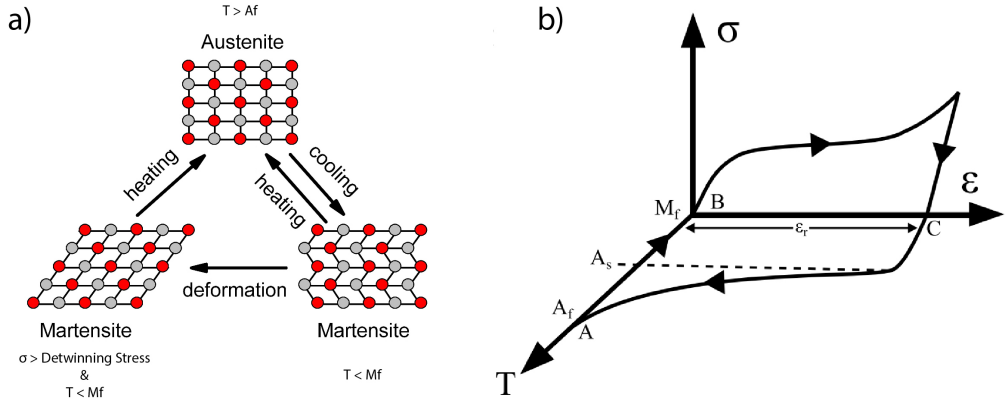

Figure 2.4: a)SME reversible solid-state phase transformation between Austenite and Martensite cycle. b) Relationship between Stress, Strain, and Temperature in SME cycle. [31]

softer twinned Martensite.

In the case of no deformation, the material transforms only between twinned Martensite and Austenite phases, and therefore, no actuation is observed. Hence, in many applications that require repeated actuation, a continuously present load is applied to the SMA actuator. For example, in many applications which an SMA actuator wire is used, a constant load or a spring continuously applies the needed load to deform the actuator. In these cases, the transformation happens only between the de-twinned Martensite and Austenite phases.

There are methods of incorporating a two-way shape memory effect (TWSME) through specific thermo-mechanical processes [32, 33, 34, 35, 36, 37, 38]. These unique materials which exhibit TWSME do not need a biasing force to deform the material. These materials revert to the deformed position upon cooling and back to the original shape when heated.

Newly fabricated SMA actuators are not inherently stable. Therefore they need to go through a thermo-mechanical stabilisation cycles known as the training process. The training process through thermal cycling of an SMA actuator is shown in Figure 2.5. It's

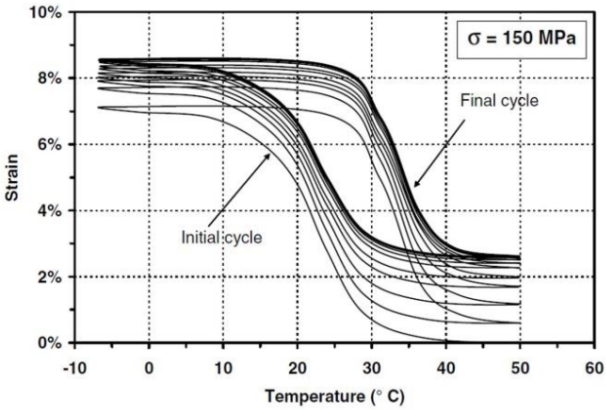

Figure 2.5: Temperature-Strain data of SME thermal cycling (50 cycles) under a constant 150MPa stress, showing the training process.[31]

important to note that the relative change between each cycle is substantially diminished after only a few cycles. This training process is performed on many different geometries such as wires, sheets, and tubes. The same process is also true about SMA material which exhibits PE behaviour which is discussed more in Section 2.1.4.

2.1.4 Stress Induced Phase Transformation & Pseudo-elastic Effect

The other very important behaviour of SMAs which is widely used in industries such as bio-medical is the Pseudo-elastic Effect (PE), also known as Super-elastic Effect. Figure 2.6 shows a typical stress-strain relationship of PE at a constant temperature.

In the phase-transformation dynamics, PE acts as the opposite force to SME. Temperature-induce phase transformation (which occurs in SME) tries to transform the material from Martensite to Austenite, however, stress-induced phase transformation (which occurs in PE) tries to transform the material from Austenite to Martensite. Both PE and SME are states of the SMA with respect to the ambient temperature which in most cases is the room

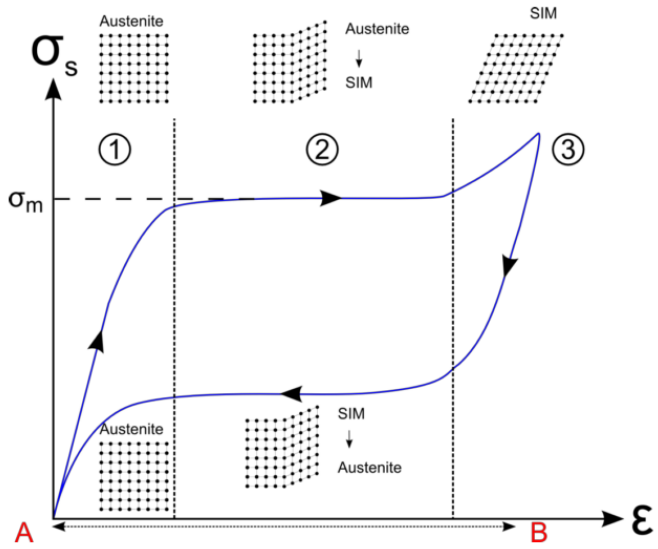

Figure 2.6: PE Stress-Strain relationship with marking related to Austenite to Martensite Phase Transformation. [39]

(or body) temperature. Therefore, one SMA material can have a PE behaviour at room temperature, and the same exact material can have an SME behaviour. This phenomena is very clearly illustrated in Figure 2.7. In fact the terms PE and SME are relative terms which indicate what the initial phase of the material is and how the transformation occurs.

Even though, PE is mostly used in passive applications (such as bio-medical orthodontics arch-wires and vascular stents), they can also be used for actuation as well. This mode of SMA actuation is called PE-actuation. This mode of actuation is achieved by straining the material (refer to Figure 2.7). There is also another mode of SMA actuation called HP-SMA actuation. This actuation is obtained by first. The mechanics of all these SMA actuation modes are very similar in nature and follows the regular PE & SME rules as outlined previously.

Similar to SME actuation, if repeatability is desired for PE actuation of as-fabricated

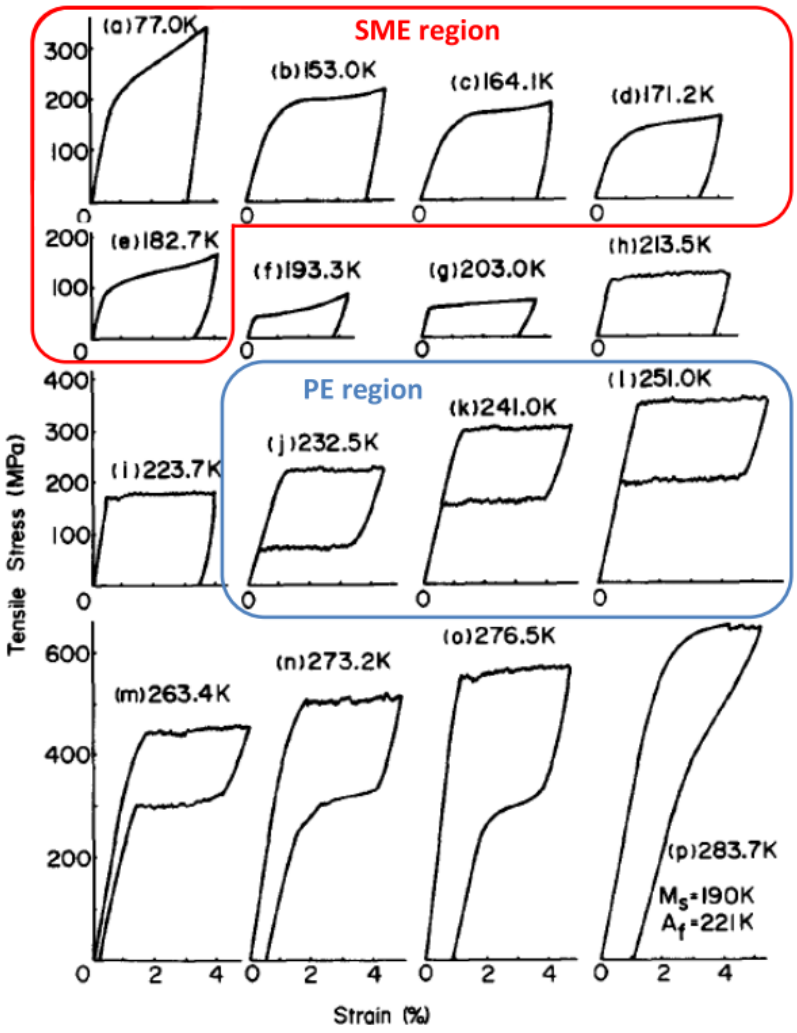

Figure 2.7: Stress-Strain behaviour of Ti-rich NiTi SMA under different temperatures; conveying the relative nature of the terms PE and SME. [28]

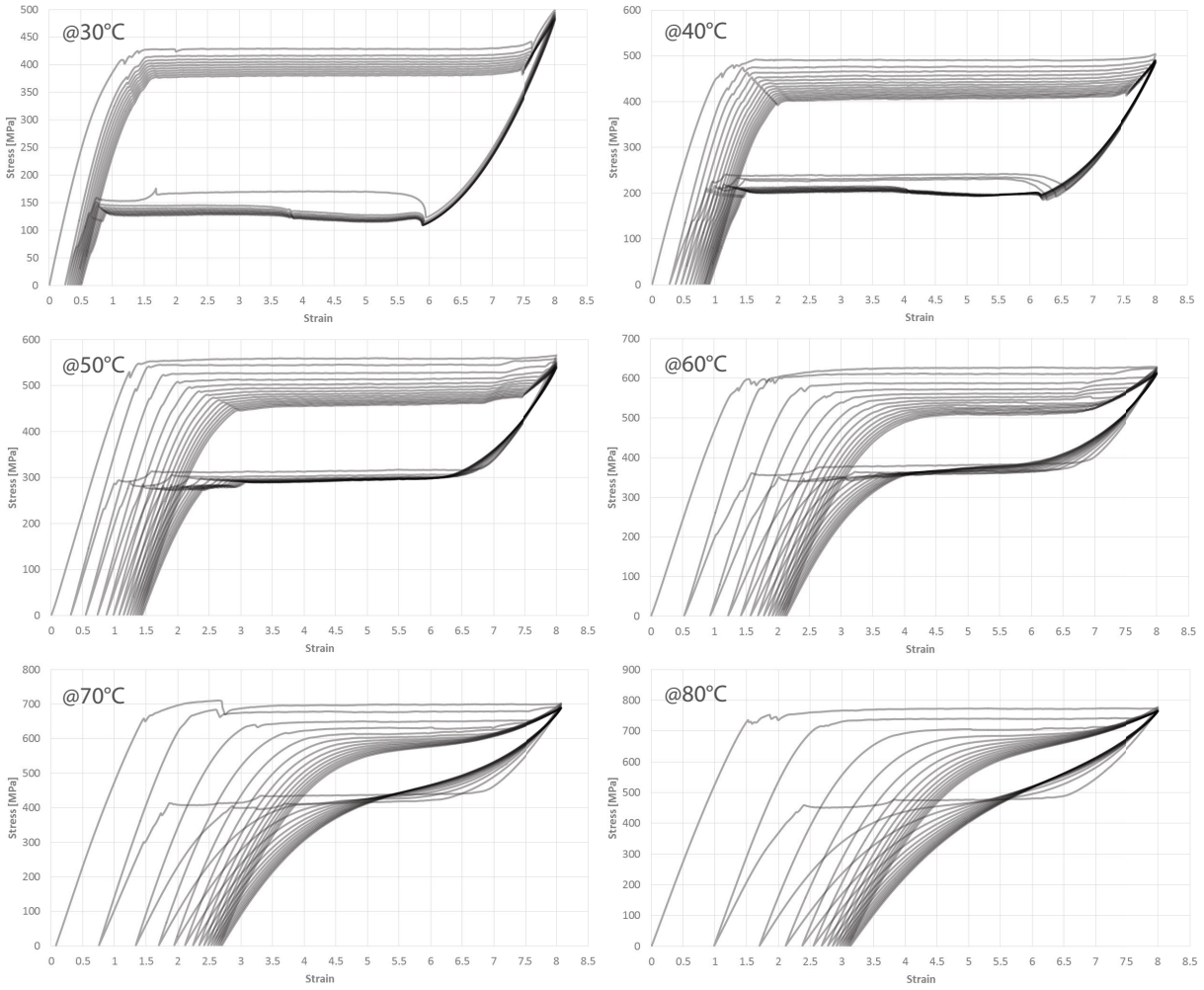

Figure 2.8: Obtained Stress-Strain data of PE NiTi SMA undergoing 15 mechanical cycles up to 8% strain at different temperatures.

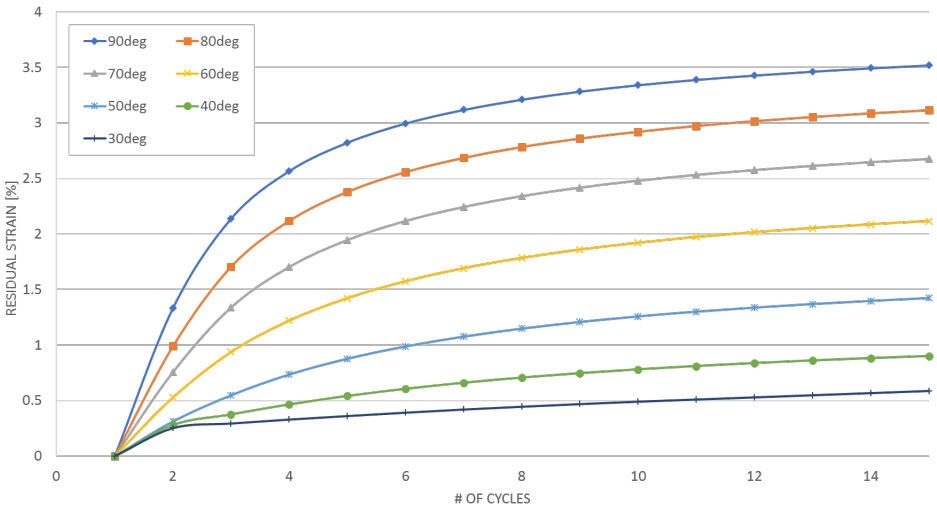

Figure 2.9: Effect of number of mechanical cycles on residual strain of PE.

SMA material, the material should undergo training process as well. This training can be performed by thermo-mechanical cycling of the material. Figure 2.8 shows the effects of mechanical cycling of a PE material up to 8% strain under different ambient temperatures on residual strain. This residual strain of the material is then plotted as a function mechanical cycle and shown in Figure 2.9. As evident by the figure, the relative residual strain decreases exponentially as the number of cycles increases.

2.1.5 Fatigue Life

Such as any other material, NiTi SMAs experience fatigue over many repeated cycles. Understanding fatigue life NiTi is crucial in actuation application where repeated thermo-mechanical cycles are expected. In SMAs Fatigue is highly dependent on the stress-strain-temperature relationship of a given application. Figure 2.10 shows a series of Fatigue data from NiTi SMAs under different conditions. As evident in the graph, fatigue life decreases significantly by with increasing strain. Double the strain of an SMA actuator would cut its

fatigue life in half. Even though SMAs can strain up to approximately 10%, in practice, 2 to 4% strain and a maximum stress of 200-300MPa are used to meet the fatigue life demand for a typical application. Even more than the strain, fatigue life is very sensitive to overheating. 50 degrees Celsius over A_f would cause a 75% decrease of fatigue life as shown in Figure 2.10 d).

Additionally, Joules heating of the wire using electrical current degrades the life of the material due to the localized differences in resistivity which in return leads to uniform heating of different places in the microstructure.

Figure 2.11 shows a general working region of the commercially available NiTi SMA, Flexinol^{TM}wire, concerning fatigue life. The results on the graph show the familiar trend: the lower the stress and strain the longer the fatigue life.

2.2 NiTi Laser Processing

In this section, the fundamentals of MMM laser processing technology are discussed. The underlying cause of the novelty of the proposed actuator design is the ability to locally laser process NiTi SMAs by preferential Nickel evaporation over Titanium. This local change in alloys composition would result in locally modified thermomechanical properties as well.

2.2.1 Effect of Nickel Composition on Material Properties

The reason modifying the composition locally is valuable is due to the substantial effect that it has on both thermal and mechanical properties of NiTi SMA. The experimental results provided in Figures 2.12 a) & b) illustrate the effect of alloy composition on the M_s transformation temperature. These experiments were performed on casted and fully solutionized samples to ensure that the effects of the microstructure and precipitates are

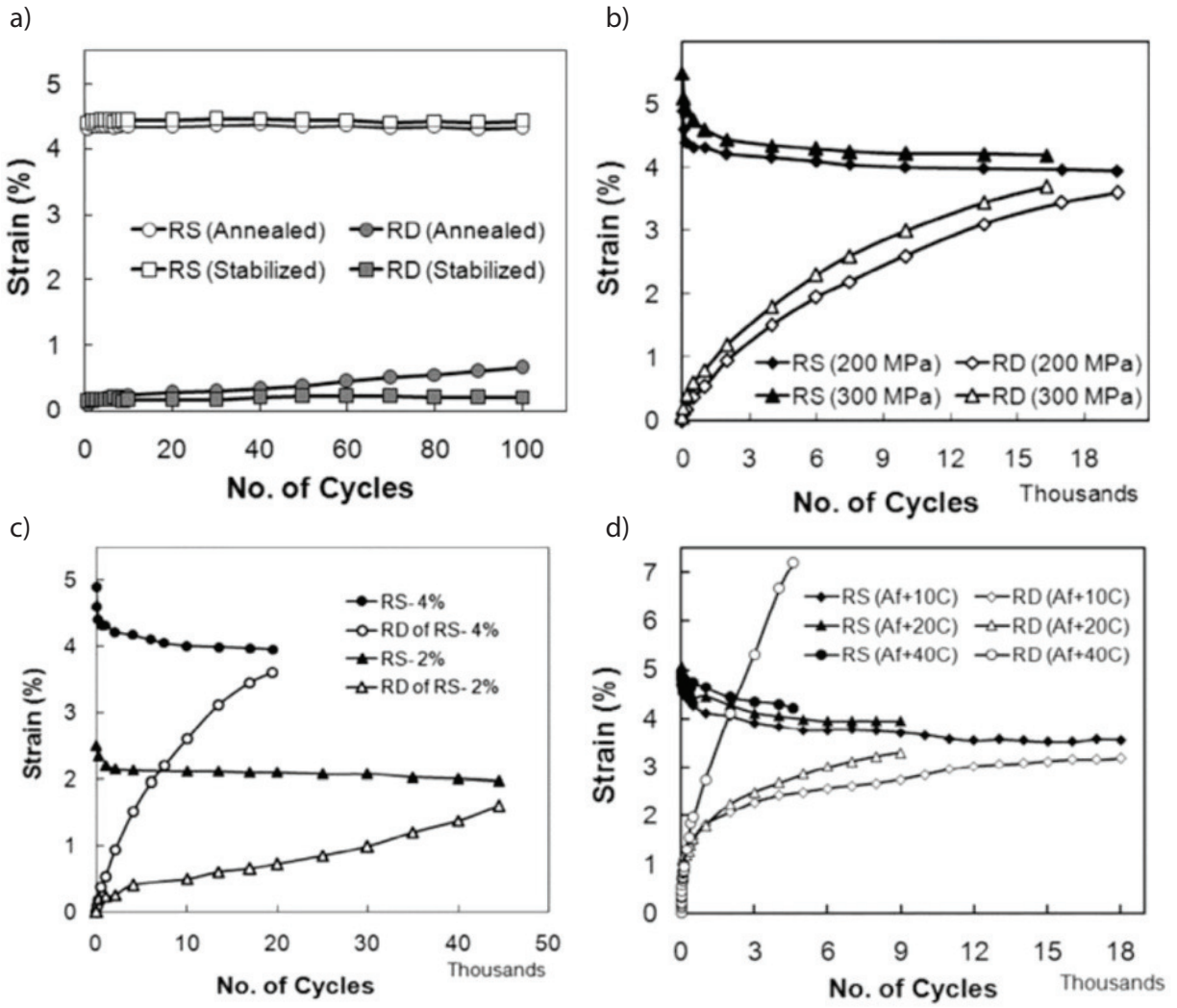

Figure 2.10: a) Strain vs. number of cycles plot upon of NiTi SMA wires under a stress of 200 MPa before and after stabilization treatment. b) Strain vs. number of cycles plot of NiTi SMA wire at 200 and 300 MPa. c) Strain vs. number of cycles plot of NiTi SMA wire at 200 MPa with actuation strain (RS) at 2 and 4%. RD is residual strain. d) Strain versus number of cycles plot showing fatigue life as a function of T_{max} in the wire; conducted at a stress of 200 MPa. [40]

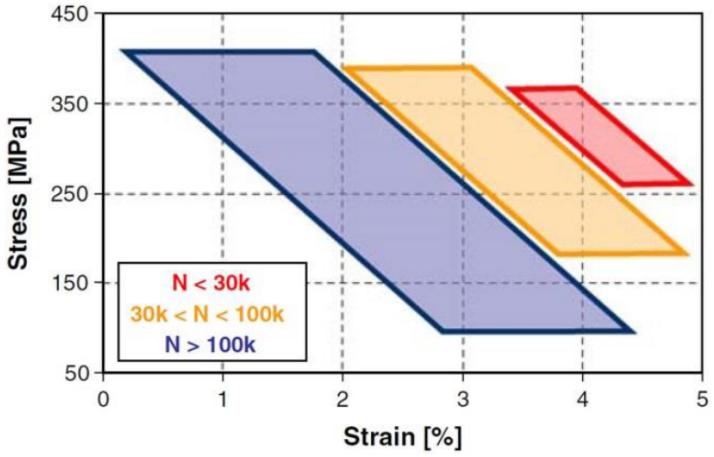

Figure 2.11: Fatigue lifetime for Smartflex^{TM}76 under different stress-strain conditions. [41]

as minimal as possible. Figure 2.12 a) shows an inverse exponential relationship between the atomic percentage of Ni and the M_s. The more Ti-rich the alloys becomes, the higher the transformation temperatures. Therefore, at a given environmental temperature, one monolithic material can exhibit both SME and PE properties at different locations of the wire.

2.2.2 Nickel Evaporation Laser Processing & MMM Technology

Pulsed Laser Nickel evaporation on NiTi was first performed by I. Khan et. al. [27] and was shown to be a very effective method of altering already existing NiTi SMA. The material processed using this approach were named Multi-Memory-Material (MMM), referring to the ability of one monolithic material actuation at different temperatures giving the capacity to remember multiple shapes. This process is different than welding or heat treating in several significant ways. To evaporate Ni form the material, a large but short pulse of laser is needed to heat up a very localized section without providing it enough

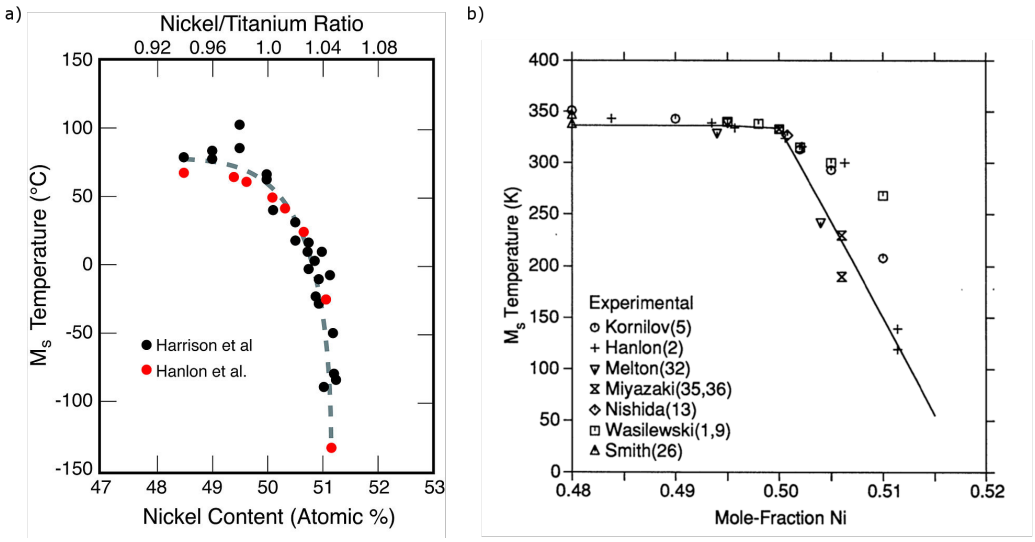

Figure 2.12: Effect of Nickel mole-fraction on the Martensite start transformation temperature of NiTi SMA taken from a)[42] b)[43].

time for the energy to dissipate to the other parts of the material. The goal is not to enter in the conduction heat transfer mode of the material. This is the main difference between heat treatment and welding, and MMM technology. MMM technology chemically changes the composition of the materials by removing Ni from NiTi alloy. The reason Ni is evaporated rather than Ti is due to the substantially lower evaporation temperature of Ni and higher partial pressure. Figure 2.13 is a graph calculated from Equations (2.1) & (2.2) along with the constant provided in the Table 2.1. It shows the comparison between the partial pressure of Ni and Ti versus different temperatures.

$$P_i = X_i P_i^0 \tag{2.1}$$

$$log_{10}(P_i^0(T)) = A + \frac{B}{T} + Clog_{10}(T) + DT + ET^2 \tag{2.2}$$

Table 2.1: Constant for calculation of equilibrium vapor pressure (P_i^0) of Ni and Ti.

	A	B	C	D	E
Ni	−214.3	−3.52E + 03	7.49E + 01	−1.80E-02	1.51E-06
Ti	−194.8742	−8.27E + 03	6.83E + 01	−1.73E-02	1.55E-06

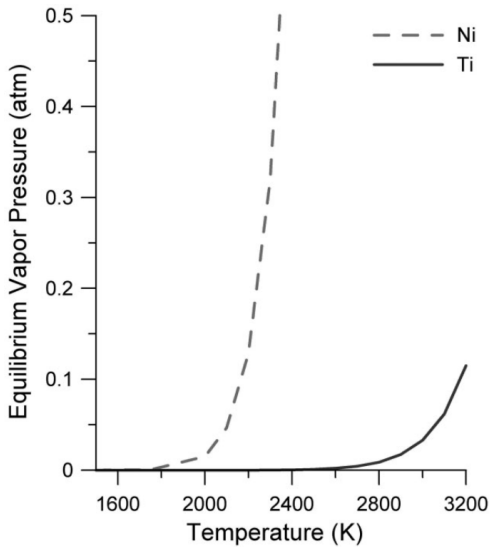

Figure 2.13: Comparison of calculated equilibrium vapour pressure of Ni and Ti at different temperatures. [44]

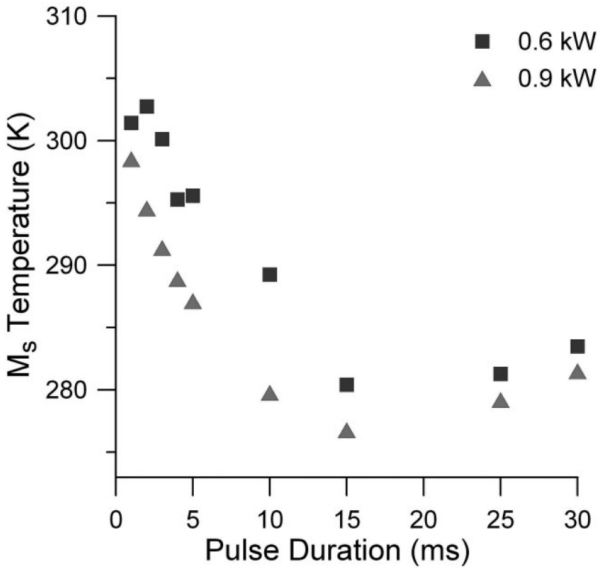

Figure 2.14: Effects of laser pulse power and duration without 0% pulse overlap on NiTi SMA on M_s transition temperature of the wire. [44]

The exact amount of Ni removed depends on many various factors such as the number of pulses per spot, pulse power, pulse duration, spot overlap. Figure 2.15 shows the effect of zero overlap single laser pulse with different pulse durations and powers. As the duration increases, the transformation temperature decreases. This might be counter-intuitive, but the more of the heat transfer is in the conduction mode which results in more Ni being dissolved in the melt pool. At the same time increase the power only increase the amount of Ni removes slight, thus slightly increasing the transformation temperatures.

Figure 2.16 shows the effect of the number of pulses per spot on the amount of atomic percent of Ni removed as well as M_s transformation temperature. It's The transformation temperature reaches a saturation point after four pulses. At this point, the SMA is very Ti-rich. Processing more pulses per spot than five causes undesirable IMCs to be produced which significantly reduces the life of the material.

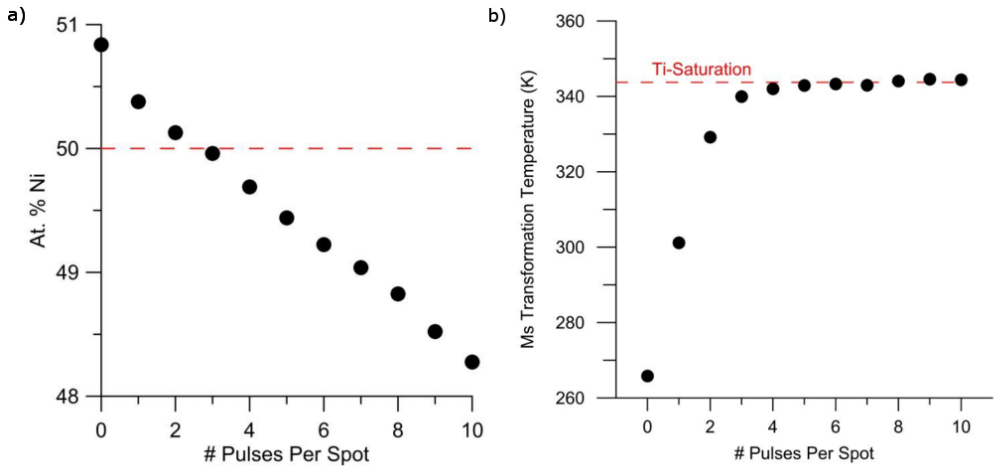

Figure 2.15: Effect of the number of laser pulses on the Martensite start M_s transformation temperature taken from [45] with modification.

Figure 2.16 an optical metallography photo of the effect of one laser pulse on NiTi SMA as-processed and after revolutionization with the Fusion Zone (FZ) and Heat-Affect Zone (HAZ) labeled. To eliminate the fusion zone, spot overlap is required, so the next pulse spot dissolves the microstructure. This would significantly improve the fatigue life of the actuator.

In this chapter, the metallurgy of NiTi and other high-temperature SMAs are discussed. Additionally, detailed explanation of phase transformation mechanism of NiTi SMAs are presented, and different properties and behaviours of NiTi under various conditions are provided. Moreover, brief discussions about the effects of stress and elongation on the fatigue life of SMA actuators are given. Lastly, the MMM laser processing technology is explained, and the theory behind laser Nickel-evaporation are presented. Using localized laser Nickel-evaporation, one could fabricate an SMA actuator which contains two entirely different properties in one monolithic wire. The fabrication of the wire is explained in more

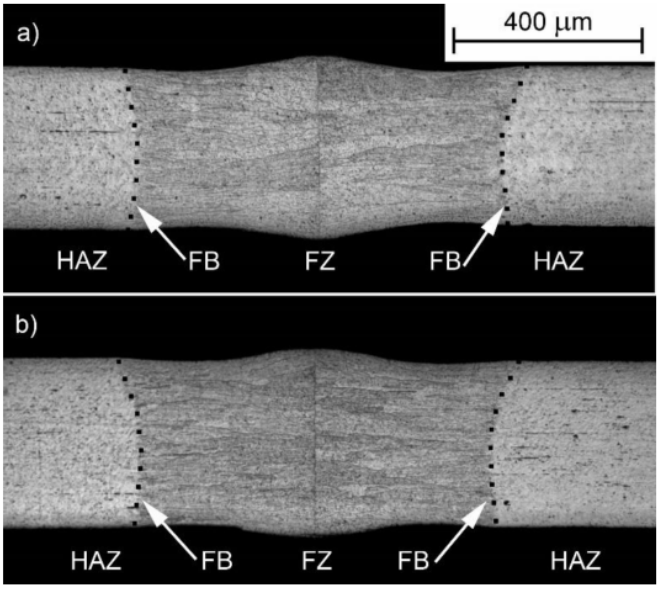

Figure 2.16: Optical metallography Photo of the effect of one laser pulse on NiTi SMA showing fusion zone (FZ) and heat-affected zone (HAZ). [45]

detail in the following chapter.

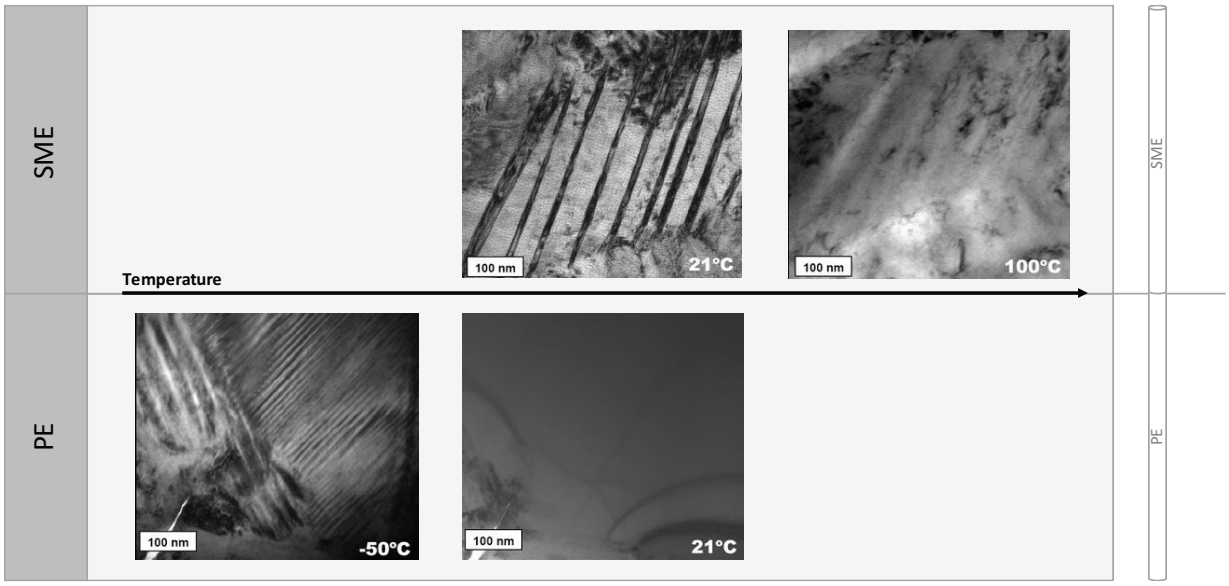

Figure 2.17: Photos of the microstructure of two different regions of MMM-processed NiTi wire showing the presence of both Austenite (PE) & Martensite (SME) phases at room temperature.

Chapter 3

Fabrication

Multiple steps were required to successfully fabricate the linear actuator. This included a unique laser processing step to tune composition, followed by a thermo-chemical treatment to achieve desired mechanical properties. The current section outlines and detail these steps.

3.1 Laser Processing

3.1.1 Setup

In this section the design of a machined which was made by the author for the purposes of continuous laser-processing NiTi wire is discussed. In addition to the design of the machine, some of the processed samples are presented and discussed.

3.1.2 Processing

Pulsed laser processing of NiTi SMA has shown to change the composition of NiTi by preferentially evaporating compositional constituents [27, 46, 28, 39, 44, 47]. This process,

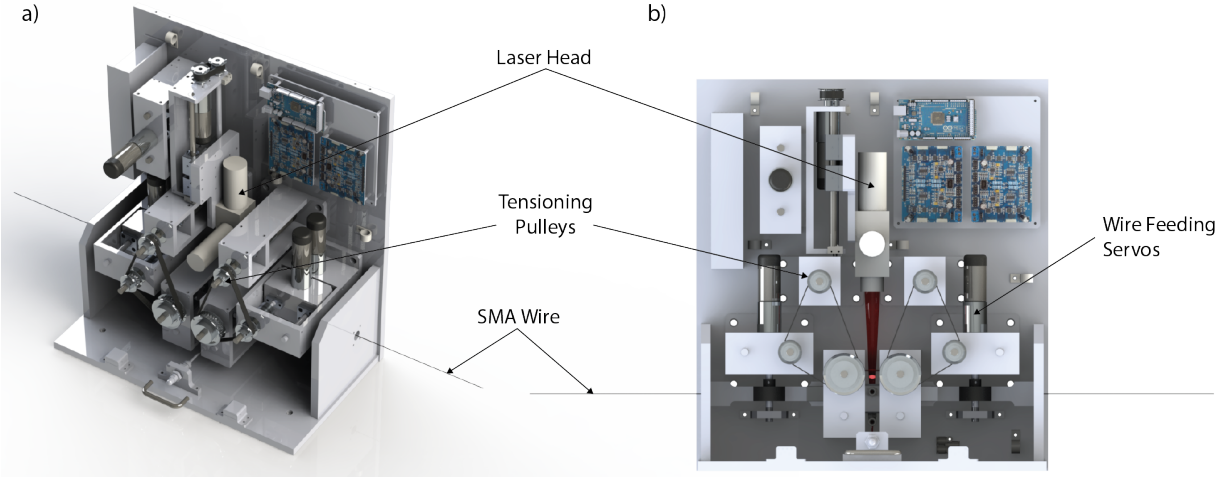

Figure 3.1: 3D renderings of Wire feeding and laser processing SMA fabrication setup used to produce the wire with dual-roller on each side and adjustable vertical tension on the wire.

called the Multiple Memory Material Technology, can drastically change the local functional properties of SMAs since they are highly very sensitive to the alloy composition. Even subtle changes (0.01 at. %) can alter the functional properties of SMA's such as transformation temperatures and pseudo-elastic stresses [48]. This technology enable the fabrication of a wire having different portions that poses unique thermo-mechanical and electromechanical properties.

Figure 3.2 demonstrates the effect of a single 5ms laser pulse power on the transformation temperatures of NiTi. It can shown that laser power has a direct impact on how much nickel is evaporated which makes it possible to control the properties of different sections of the wire by controlling the amount of power. In addition to laser pulse power, laser pulse time and laser spot overlap have an effect on the properties as well, however the effects of these laser processing parameters are beyond the scope of this paper and will be detailed in a future study [ore refer to existing studies, i.e my paper... that way the reviewer wont

say you need to do that first]. Every pulse is 60% overlapped on the previous pulse in order to remove the previous solidification line. Figure 3.7 a) shows a magnified photo of a LP NiTi wire and illustrates the boundary between the original Base Metal (BM) and Laser Processed (LP) region.

Before laser processing the BM wire is cleaned using Ethanol and Acetone to remove any impurities on the surface. Then, the BM wire is laser processed in a continuous fashion as shown in Figure 3.6 using a computer controlled roller system. Only the places that need to have SME properties were processed. In order to prevent oxidation, the wire was purged inside an argon gas chamber during processing. For the proposed actuator design in this paper, a single 1000W 5ms pulse was used. Figures 3.8 a) & b) show the DSC results of BM and LP wire.

3.2 Effects of Laser Parameters

In previous studies, as discussed in the Literature Review chapter, effects of overlap of laser spots were studied. However, the effects of the laser power and pulse duration were never explored. In this section, the effects of Laser Pulse Power and Pulse Time on the transformation temperatures of the NiTi SMA is presented and discussed.

Approximately ten different laser pulse powers ranging from 700W to 1200W with three different laser pulse times of 4ms, 5ms, and 6ms were pulsed on 450um diameter Nickel-rich SE908 NiTi wire with 60% laser spot overlap. The resultant transformation temperatures obtained from DSC tests are shown in Figures 3.2 b), 3.3 b), and 3.4 b).

As evident from the results, the amount of nickel evaporation increases as the laser pulse power increases which leads to a NiTi material with higher transformation temperatures. There is a limit to how much removal of Ni can affect the material properties. At this point

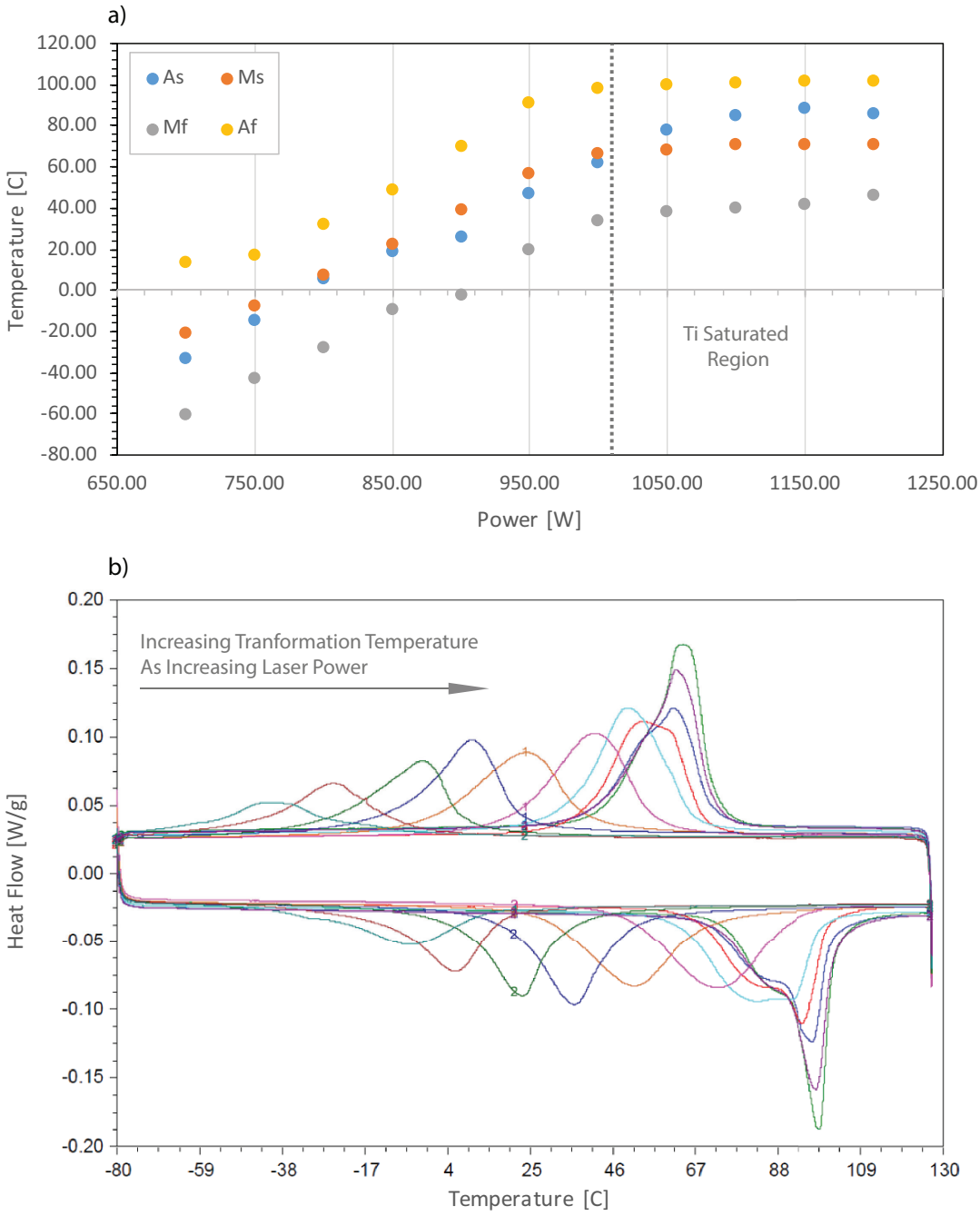

Figure 3.2: 6ms laser pulse time: a) Effects of laser power on phase transformation temperatures of laser processed NiTi, noting the Ti-rich saturation region. b) DSC results showing the range and convertibility.

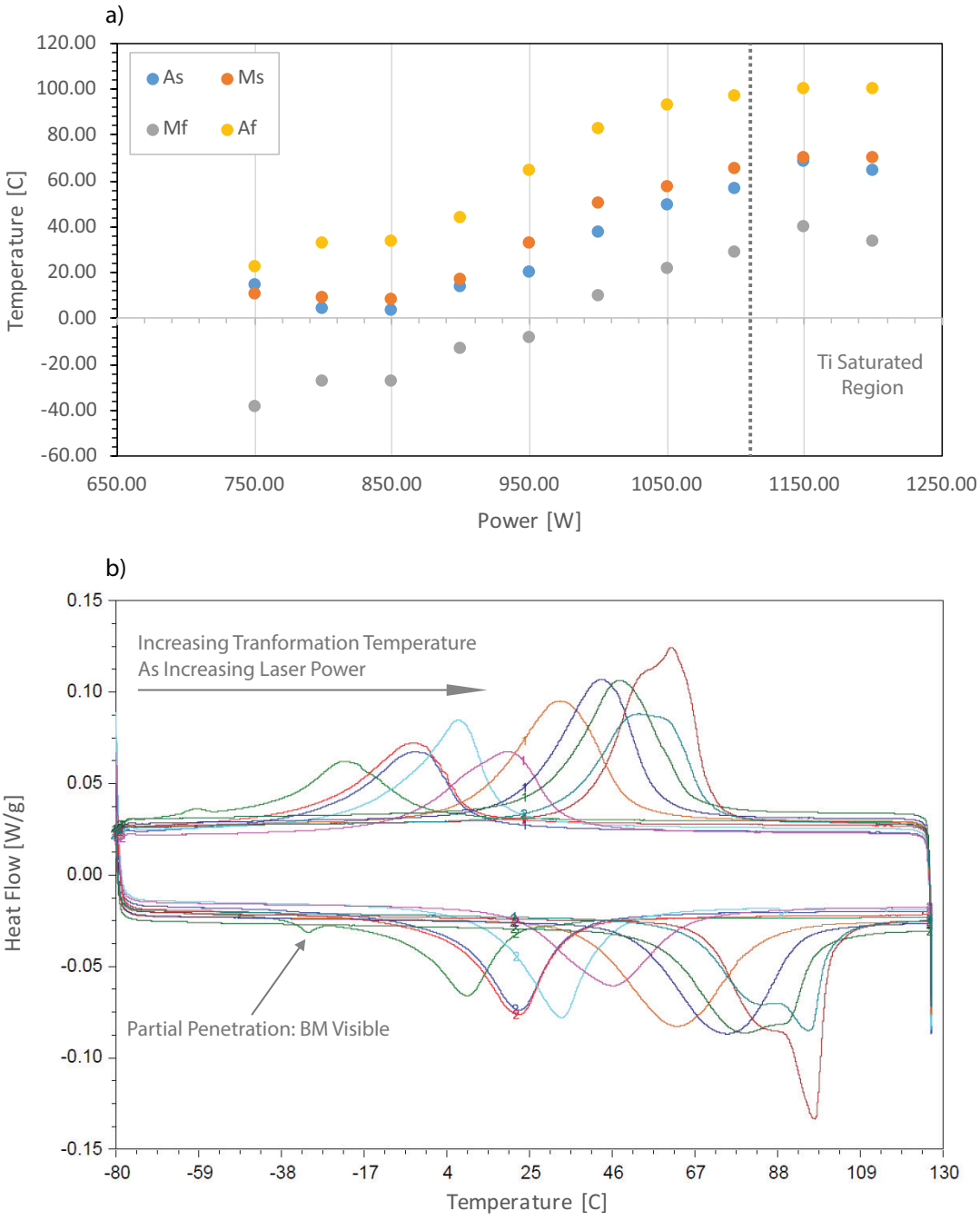

Figure 3.3: 5ms laser pulse time: a) Effects of laser power on phase transformation temperatures of laser processed NiTi, noting the Ti-rich saturation region. b) DSC results showing the range and convertibility.

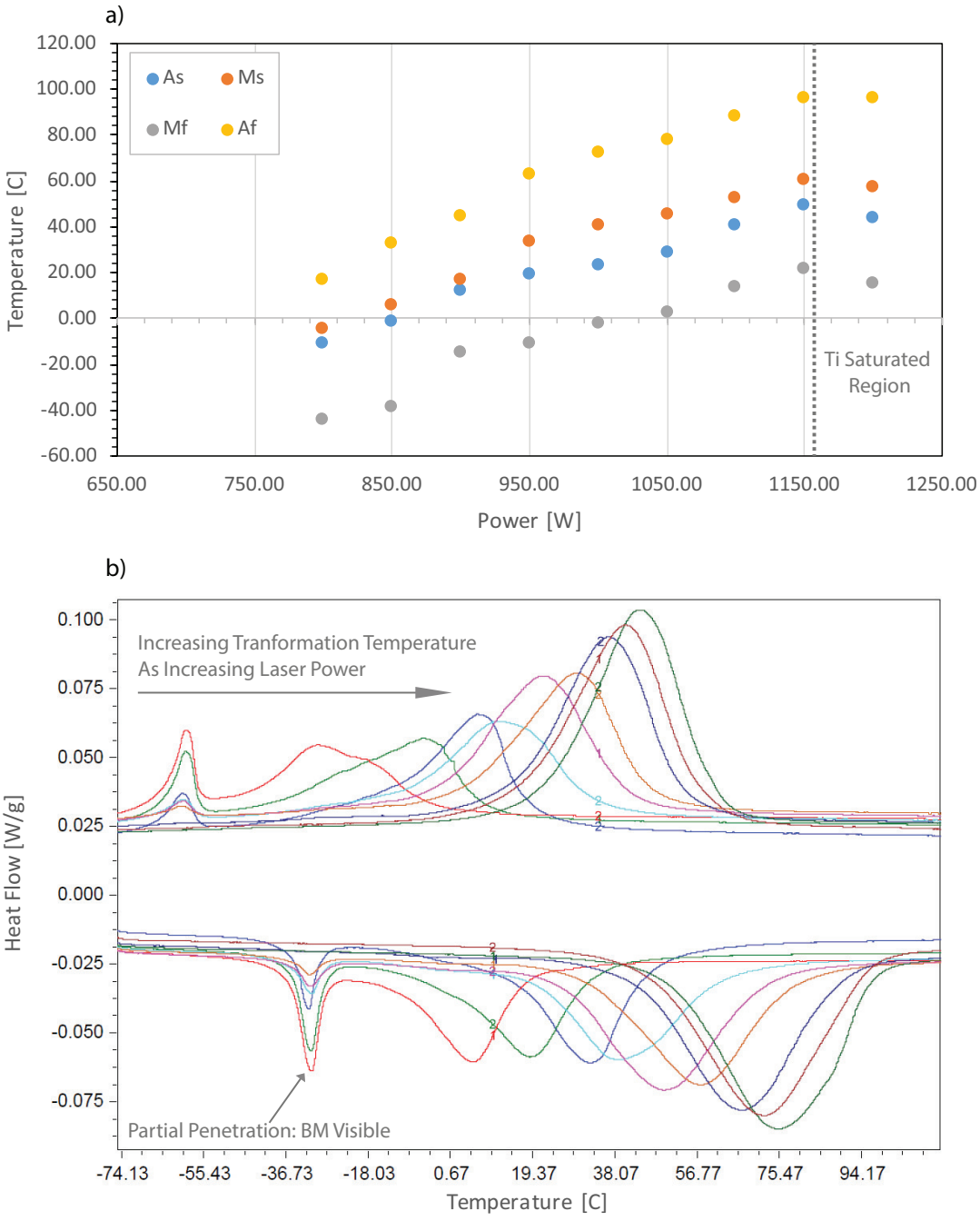

Figure 3.4: 4ms laser pulse time: a) Effects of laser power on phase transformation temperatures of laser processed NiTi, noting the Ti-rich saturation region. b) DSC results showing the range and convertibility.

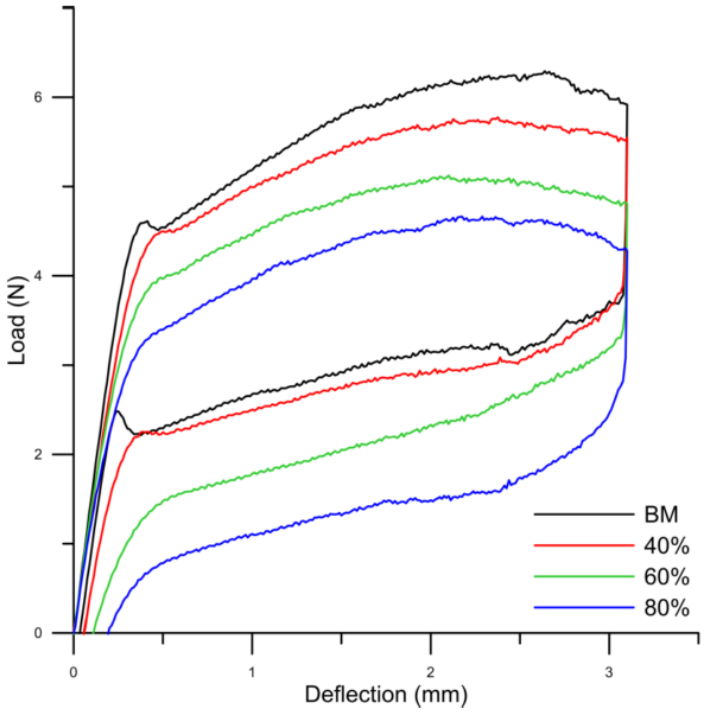

Figure 3.5: Effect of increasing laser pulse powers on a three point bend tests of PE SMA wire [39].

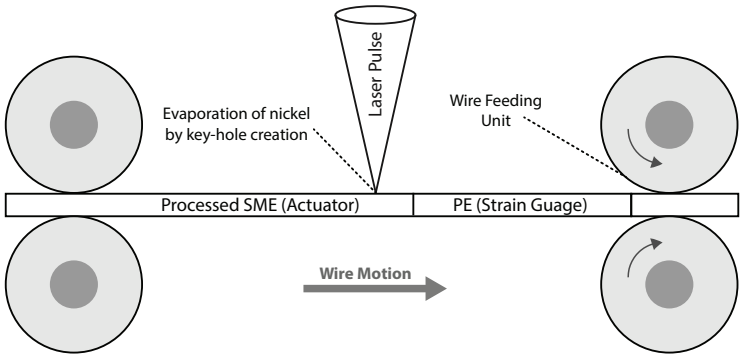

Figure 3.6: Laser processing schematic showing the continuous arrange of processing suitable for mass production.

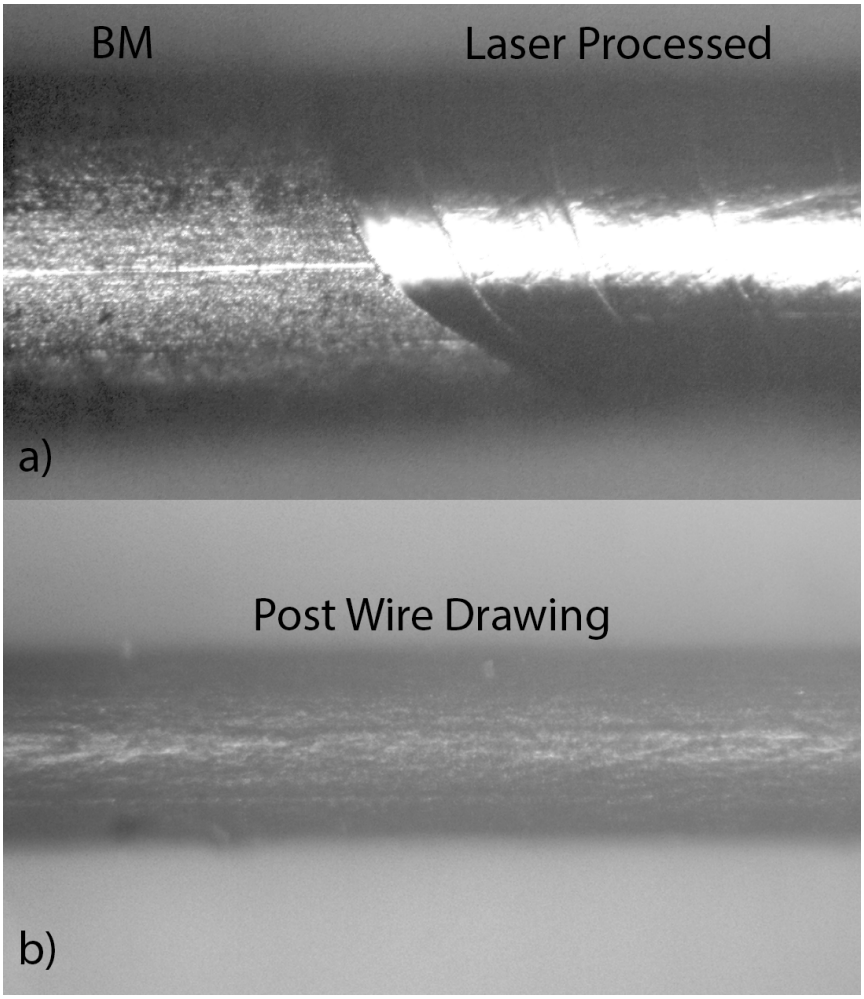

Figure 3.7: (a) Laser-processed NiTi wire showing the processed region and the BM. (b) thermo-mechanical Treated Wire showing the uniformity of texture between BM and LP region.

(saturation region) the transformation temperatures do not increase anymore. However, the removal of Ni causes the formation of Ti-rich secondary intermetallic phases in the material which adversely effects the properties. Therefore, it is not recommended to over saturate the material with Ti. These saturation regions are illustrated in Figures 3.2 a), 3.3 a), and 3.4 a) by a dotted line.

Based on these results, it could be expectantly observed that the effect of laser pulse power on transformation temperatures is greater the larger the laser pulse time is. Additionally, one more interesting observation could be made on the results of the 4ms laser pulse time. At this pulse time, the lower pulse powers do not have the necessary amount of energy to penetrate through the material which results in Ni-removal from only a portion of the cross-section of the material. This could be seen in the DSC results presented in Figure 3.3 b) (indicated by an arrow) where for the lower pulse powers there are two peaks, one for the unprocessed base metal, and one for the Ni-evaporated region. These results are significant because as mentioned in Chapter 1, up until these results it was though that the only ways to modify the transformation temperatures are by changing the amount of laser spot overlap or by increasing the number of laser pulses per spot.

3.3 Thermo-mechanical Treatment

thermo-mechanical treatments of the laser processed wires are crucial for the final microstructure and properties of the actuator. It is important to note that various heat treatments have an effect on the transformation temperatures and mechanical properties of SMA as well [49, 50, 51, 52, 53, 54]. Laser processing significantly alters the wire microstructure; hence, after laser processing the wire is solution annealed at $1000°C$ for 1 hour. The wire is subsequently drawn though several dies in order to refine the grains struc-

ture and induce dislocations through work hardening. The wire drawing process reduces the diameter of the wire from the initial 460 micrometers to 250 micrometers. In order to prevent excessive work-hardening and breakage, the wire was inter-annealed at $600°C$ for 15 minutes after every three dies [45]. Upon completion of wire drawing step, a final heat-treatment is implemented at $480°C$ for 2 hours. At this stage of the thermo-mechanical treatment, the SMA actuator has a PE and SME portion as described in Introduction section. Figure 3.8 C) shows the transformation temperatures after thermo-mechanical treatment, and Figure 3.7 shows the wire drawn actuator wire. After wire drawing there is no longer a visible boundary between the BM and LP regions. However, the properties of the actuator need to be stabilized, which is achieved through a training processes.

Typically there are different types of training: iso-thermal stress cycling [38], iso-stress thermal cycling [55], or a combination of thermal and stress cycling. Training process induces directionally preferential martensite variants in the microstructure of the material [37, 34, 56]. For the actuator proposed in this paper, an approximately 1000 isostress thermal cycles were performed to train the proposed fabricated SMA actuator. After training the diameter of the wire was reduced from 250um to approximately 226um. The difference in the transformation temperatures of the pre- and post-training can be seen in Figures 3.8 C) and D).

It's important to note that the majority of current publications study a commercially available NiTi SMA known as Flexinol. Therefore, because of the difference in alloy composition and it's thermo-mechanical history, many of the mechanical and electrical properties of the proposed actuator presented in this paper are different from existing literature although the overall behaviour is very similarly. For the current work, most of the wire properties were determined experimentally.

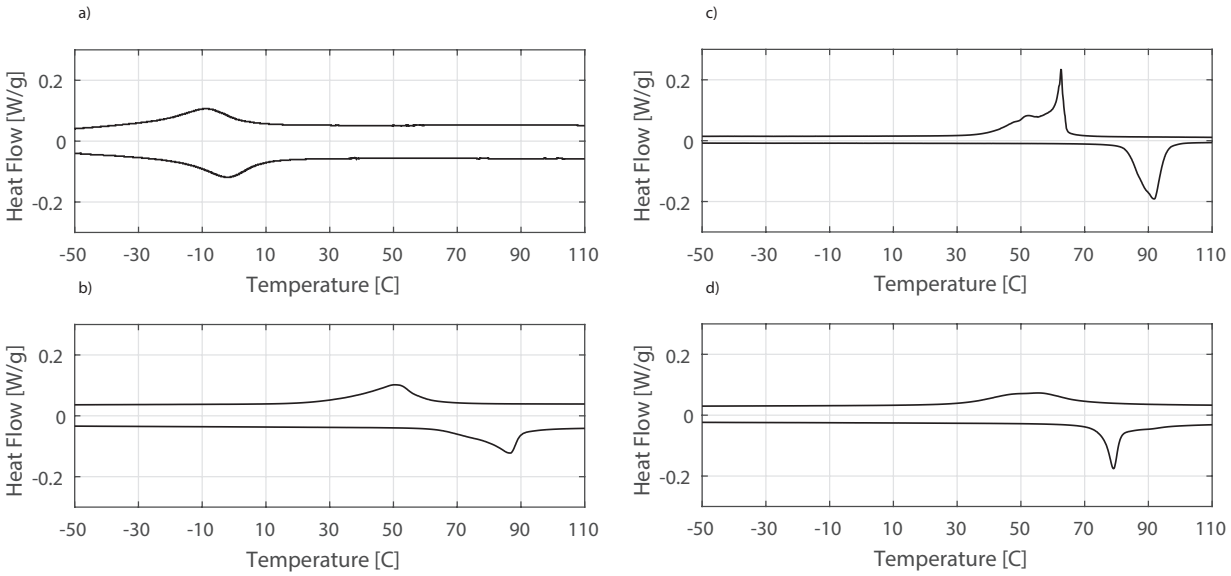

Figure 3.8: DSC results showing the phase transformation temperatures of a) base metal (and PE) b) laser processed c) post-thermo-mechanical treatment d) post-training

Chapter 4

Experimental Test Setup & Electronics

An experimental setup was designed for characterization of the SMA actuators electro-mechanical properties. Figures 4.1 a) & b) show the picture and operational schematic of the experimental setup. The setup was equipped with a toque-controlled servomotor to apply dynamic load to the wire; however, for the purposes of this research only static weights were used. The actuator wire was clamped between two stainless steel plates at each end. The weights were connected to the bottom clamps. The wire was restricted to experience only vertical motion (torsional motion is restricted as well) using a linear spline bearing. Even though the linear bearing was well lubricated, the effects of friction in the bearing was present. As such, even with constant weights, the actual stress applied to the wire is not constant. In fact, the stress applied to the wire is a combination of acceleration forces, frictional forces, and gravitational forces (weights). The setup is enclosed in a plastic environment (not shown in photo) to prevent chaotic and random air streams in the uncontrolled environment to have an effect on the convective coefficient of the wire. The experimental setup was also equipped with sensor, including high precision position incre-

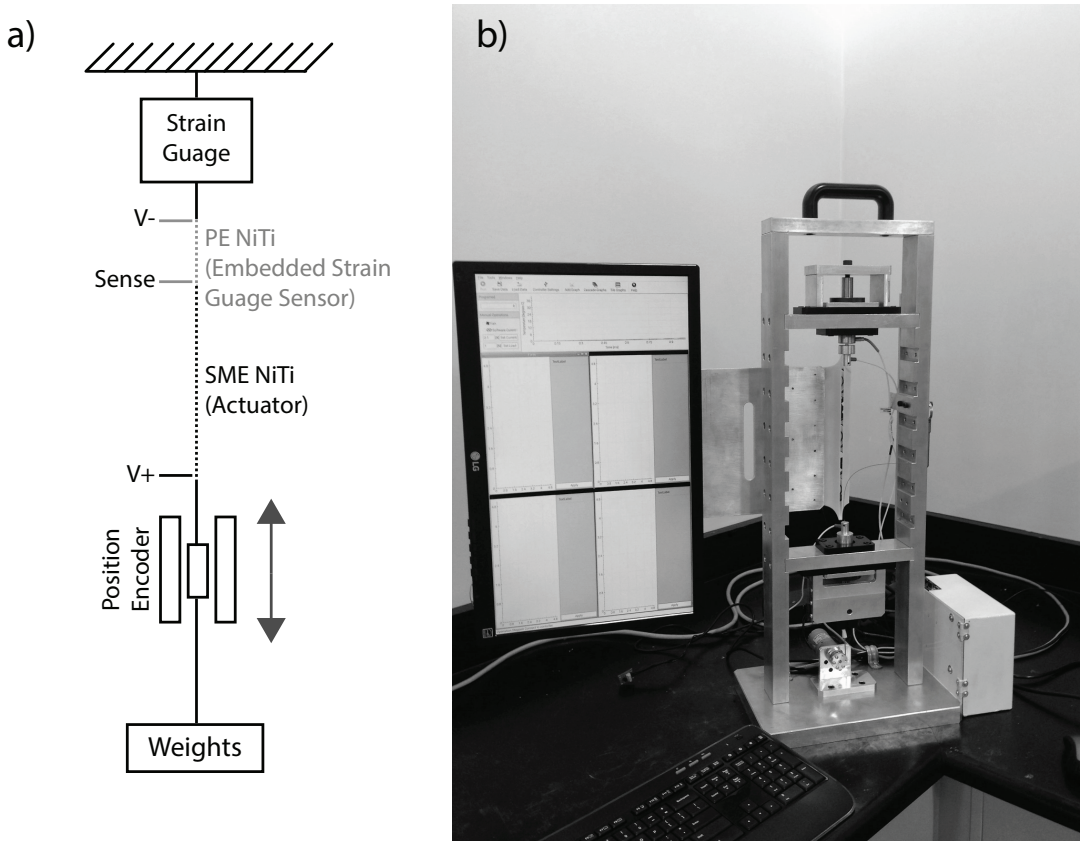

Figure 4.1: a) Operational schematic of the experimental setup. b) Photo of standalone Portable Experimental Setup.

mental optical position encoder, load cell, and precision ambient temperature sensor. The electrical circuitry that is responsible for data acquisition and control of the experimental setup is detailed in the following section.

4.1 Current Driver & Measurement Circuitry

Heating of the wire was achieved through joules heating. In order to control the wire temperature, and subsequently its position, a variable and controllable power supply was

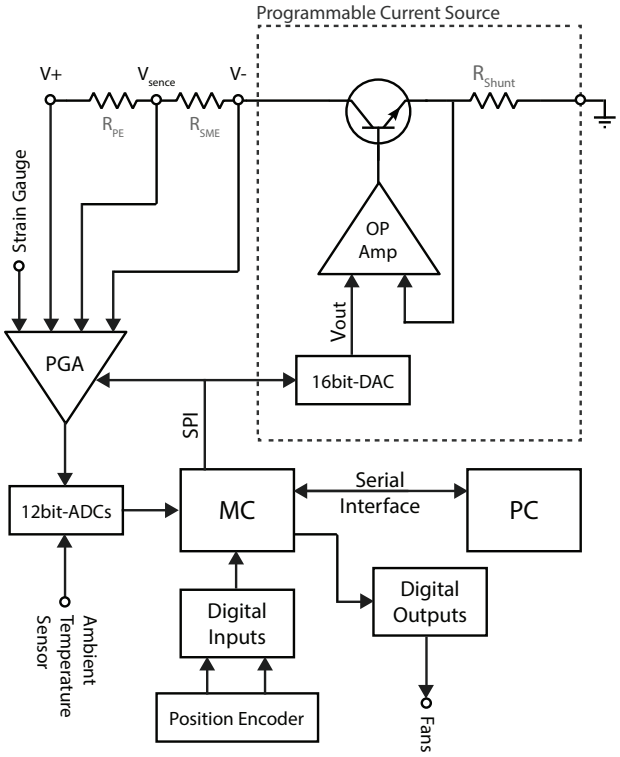

Figure 4.2: Electrical schematic of the SMA actuator driver circuitry.

needed. Since the purpose of the current study is to estimate the position of the actuator in a sensor-less fashion using two resistance measurements, the circuit had to be able to measure two resistances very accurately. The implemented circuit was a controllable current source, and its simplified electrical schematic is shown in Figure 4.2.

The current source was implemented using a high gain darlington bipolar junction NPN transistor. The transistor was located in a sinking configuration with respect to the electric load (actuator). A low-side current sensing shunt resistor is used to measure the current and feed it back to the negative input of a difference amplifier connected to the transistor. A 12bit digital to analogue converter (DAC) is connected to the positive input of the difference amplifier and acts as the reference (commanded) current signal. This hardware

feedback loop runs at 5 MHz and tries to keep the commanded current constant under changing electrical load (actuator's resistance).

Resistance was calculated by measuring the current through the wire and measuring the respective voltage drop as shown in Equations 4.1 & 4.2. The parameters of the equations are labeled in Figure 4.2. The measured current comes from the shunt resistor as described earlier. The two voltage drops across the PE and SME portions are measured using a high Common Mode Rejection Ratio (CMRR) of 140 dB differential Programmable Gain Amplifier (PGA). High CMRR is essential when measuring very small differential voltages as in the case of the PE portion of the actuator, the higher the CMRR the better the signal to noise ratio. The gain of the PGA is selected from the microcontroller (MC) using Serial Peripheral Interface (SPI) protocol. High amplification gain was used for more sensitive measurements such as the voltage across the PE portion. Similar to the gain, PGA contains a multiplexer and has 8 inputs which each pair can be selected for a differential via the SPI serial communication as well. In order to obtain higher effective resolution from the ADC, a technique called oversampling is used. Oversampling takes very fast consecutive analog to digital conversion and averages the converted values, therefore there is a trade-off between resolution and conversion speed [57]. The output of the PGA is passed on to a 12bit Analog to Digital Converter (ADC), and the converted digital values are sent to MC. Additionally, in order to obtain not only precise but accurate voltage measurements, the ADC uses a precision voltage reference, and it's conversions are calibrated for offset and gain errors using a secondary precision voltmeter [58].

$$R_{SME} = \frac{R_{shunt}(V_{sense} - V_{-})}{V_{shunt}} \tag{4.1}$$

$$R_{PE} = \frac{R_{shunt}(V_{+} - V_{sense})}{V_{shunt}} \tag{4.2}$$

The circuit also obtains other measurement data from the experimental setup such as actual stress using a strain gauge sensor, position of the actuator using a high resolution incremental optical encoder, ambient temperature, and input voltage to the system.

As evident from Equations 4.1 & 4.2, the lower the current the higher the noise of the calculated resistance. In order to filter potential noises, the measured current and voltages were initially filtered by a median filter and a moving average filter. MC was connected to the PC using RS232 serial interface. All the measured data including time is sent to PC for logging. MC is running at 200Hz of frequency, and all the filtering and signal processing is performed in real-time on the microcontroller. Obtained position and electrical resistance of SME under different applied stresses can be seen in Figure 4.3.

4.1.1 Software

A software was written in C++ in order to communicate with the control board. It also receives, logs , and visualizes the measured data. The software uses the Qt open source C++ framework to facilitate many of the functionality. Additionally, there is a graphical user interface (GUI) which facilities the use of the testing setup. A screen-shot picture of the software is presented in Appendix A. The communication between the software and the control board is done using RS232 serial communication protocol via a USB connection. The data is transferred at a relatively high Baud rate of 115200 bits/sec. All the control and calculations are performed on the controller side for real-time performance purposes. Therefore, the software is used mostly for logging, visualizing, and human-to-setup interface.

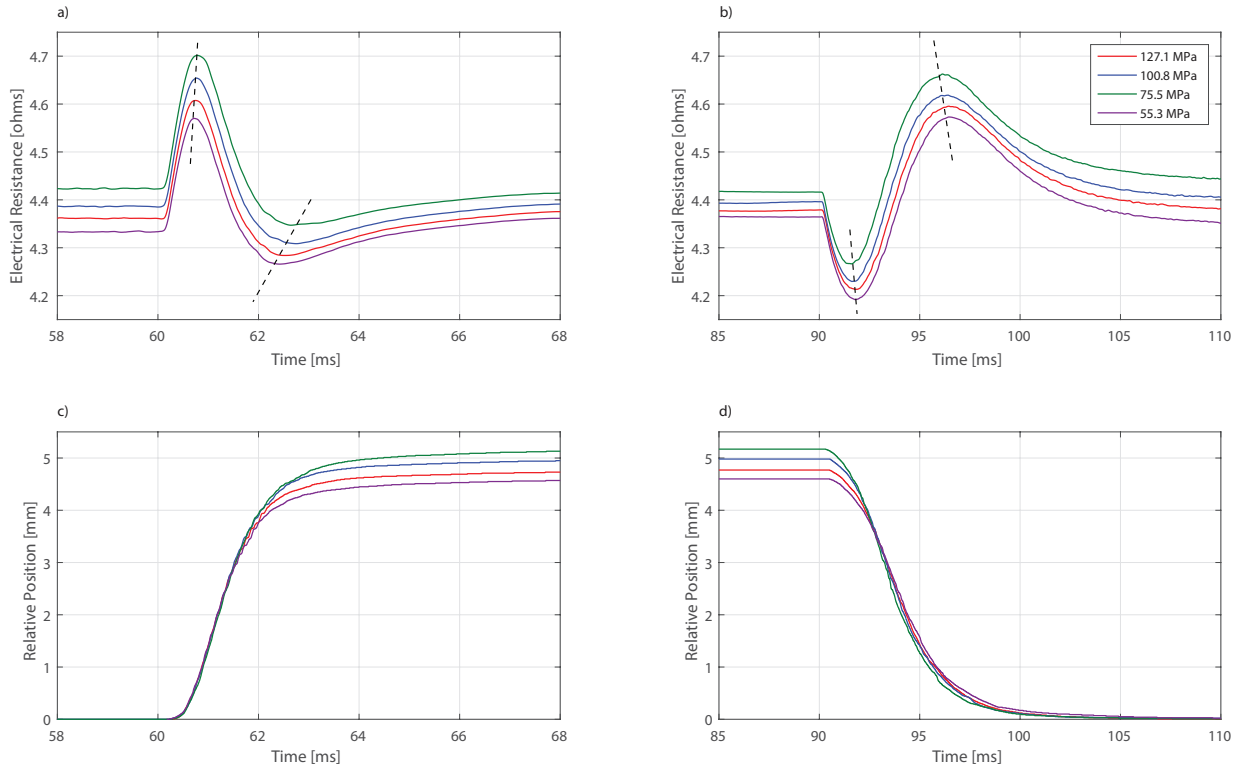

Figure 4.3: Raw data acquired from the electrical circuitry after applying noise cancellation filters: a)Electrical resistance during heating (martensite to austenite) b) electrical resistance during cooling (austenite to martensite) c) position during heating d) Position during cooling

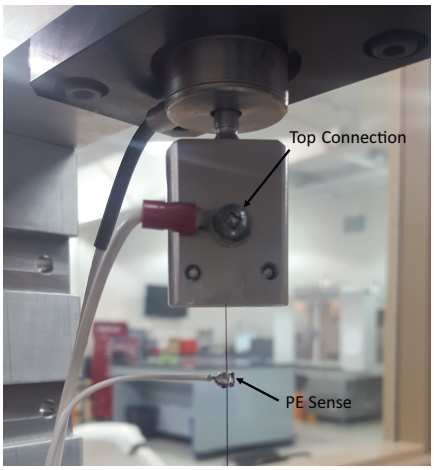

Figure 4.4: Photo of top electrical connection showing the stainless-steel plates & the middle sense probe.

4.1.2 Electrical Connections

As previously mentioned, each end of the actuator wire was clamped between two stainless steel plates; and subsequently, the plates are connected to ring terminals that create an electrical connection between the current source circuitry and the actuator wire. For these purposes, a wire was soldered to a copper rod which was crimped to the PE portion of the Actuator. This connection was used for the middle sense signal. The top electrical connections are shown if Figure 4.4.

To calculated the true resistance of the actuator, and not the electrical connections and wiring, the resistances from the circuit to the connections was measured using a 4-wire resistance measurement technique to be 0.32 ohms.

In this chapter, the experimental setup, the electronic circuit, and computer software used in the experiments are discussed. The method behind measuring the voltages and calculating resistances are discussed along with the connection of the wires, especially the

middle prob. Finally, some raw experimental data were presented in Figure 4.3. Based on these data, it can be seen that the resistance of an SME wire changes both based on temperature and stress; therefore, it's physically impossible to estimate the position of SMA actuator using only one resistance measurement under unknown stress. This creates the motivation for an algorithm to estimate the position (or force) of the wire. This position estimation algorithm is discussed in detail in the following chapter.

Chapter 5

Position Estimation

5.1 Actuator Design Configurations

The proposed linear actuator design comprises of a single wire that has two distinct sections having different alloy compositions. A larger section facilitates actuation while a smaller section is used for sensing stress. Therefore, both actuation and stress sensing can be achieved in a monolithic SMA wire. The design of the actuator is shown in Figure 5.1. The embedded sensor has transformation temperatures lower than the operating temperature, allowing it to exhibit PE properties. The effects of temperature on the pseudo-elastic behaviour is shown in Figure 5.2. In this actuator design the applied stress must remain below the pseudo-elastic plateau at any given temperature. This helps ensure operation

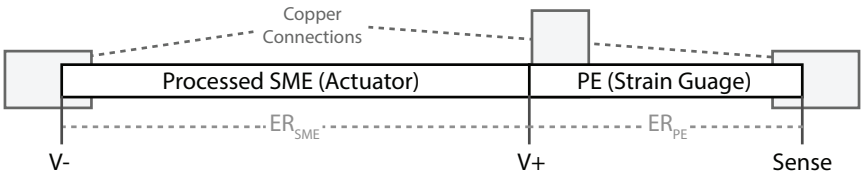

Figure 5.1: Laser processing schematic showing the continues arrange of processing suitable for mass production.

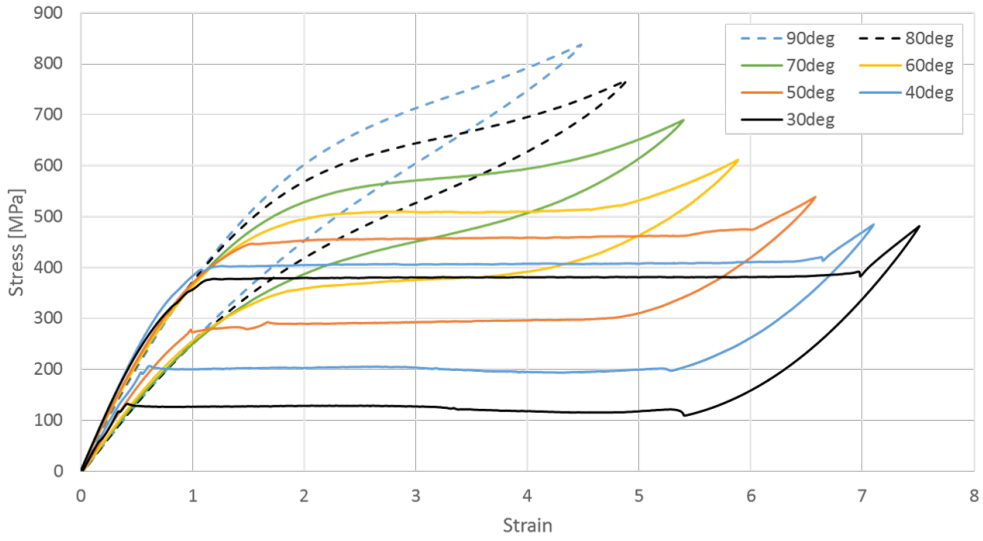

Figure 5.2: Experimental results showing effect of temperature on pseudo-elastic plateau on a trained pseudo-elastic NiTi wire.

is within the elastic deformation of the austenite phase, which remains very constant and relatively linear at different temperatures.

The actuation region has regular SME properties which has higher transformation temperatures than the initial operating temperature and PE region. There are two major electrical configuration of the proposed design. One configuration has the electrical current going through both PE and SME regions thus heating both sections; the other configuration has majority of the current going through the SME region only. Both of these configurations are valid, however, in the Part I of these series of papers the latter configuration is chosen.

5.2 Electromechanical Properties & Modeling

A thermal model of the actuator wire was developed in order to obtain temperature-dependent material properties. After obtaining the material properties, they were used in a phenomenological model to describe the behaviour of PE and SME sections. Properties of SME and PE portions can be found in Tables 5.1 and 5.3.

5.2.1 Simulating Temperature

Resistance properties of SME and PE are heavily dependent on the temperature of the wire. Due to the fine wire diameter (226um), measuring the temperature accurately and directly is very challenging using traditional techniques and tools, such as thermocouples and thermal cameras. Hence, temperature of the actuator was instead simulated. The simulation is made using PDE toolbox library in MATLAB based on the fundamental heat transfer parabolic PDE (Equation 5.1) [59] given the measured resistance, elongation, input current, and ambient temperature. This method of using mathematical heat transfer models to infer the temperature of the SMA actuator wire has also been performed by mat researchers such as Shu et. al. [60] and others [61, 62, 15]. However, most of these studies used a simple lumped capacitance approach to simplify the problem. Using a more complex simulation, as presented below, can provide a more accurate results especially since there are more than one material composition with different thermal properties.

$$\rho C \frac{\partial T}{\partial t} - \nabla \cdot (k \nabla T) = q \tag{5.1}$$

The actuator wire is considered to be a cylindrical body; therefore, axisymmetric with respect to its length. The Equation 5.1 can be written in cylindrical coordinates as shown in Equation 5.2.

$$\rho C\frac{\partial T}{\partial t}-\frac{1}{r}\frac{\partial}{\partial r}\left(kr\frac{\partial T}{\partial r}\right)-\frac{1}{r^2}\frac{\partial}{\partial \theta}\left(k\frac{\partial T}{\partial \theta}\right)-\frac{\partial}{\partial z}\left(kr\frac{\partial T}{\partial z}\right)=q \tag{5.2}$$

Joules heating is modeled as internal heat generation $\left(q=I^2R(t)\left(\frac{1}{AL(t)}\right)\right)$. Assuming radius is constant and thermal conductivity changes are very small ($\frac{\partial T}{\partial \theta}=0$) Equation 5.2 simplifies to:

$$r\rho C\frac{\partial T}{\partial t}-kr\left(\frac{\partial^2 T}{\partial r^2}+\frac{\partial^2 T}{\partial z^2}\right)=I^2R(t)\left(\frac{1}{AL(t)}\right) \tag{5.3}$$

where r, z, ρ, C, k, T, I, R, L are radial direction, direction along the length, density, thermal Capacity, thermal conductivity, temperature, current, resistance, and length respectively. Current, resistance, and length of the wire is provided to the simulation from experimental results. Thermal capacity was obtained from DSC tests as a function of temperature to represent the phase transformation under stress-free state. Transformation temperatures of NiTi are a function of applied stress and increase as applied stress increases. The increase of the transformation temperatures were assumed to be linear in nature [63, 64, 65] with respect to stress. This change in transformation temperatures must be accounted for when modeling SMA actuators, especially when dynamic loading is anticipated, and it's modeled as following:

$$\begin{aligned} M_{s,f}(\sigma) &= C_M\sigma + M^*_{s,f} \\ A_{s,f}(\sigma) &= C_A\sigma + A^*_{s,f} \end{aligned} \tag{5.4}$$

The constants C_A & C_M were obtained empirically based on experiments conducted in steady-state conditions. Only M_s and A_s are found experimentally, M_f and A_f are assumed

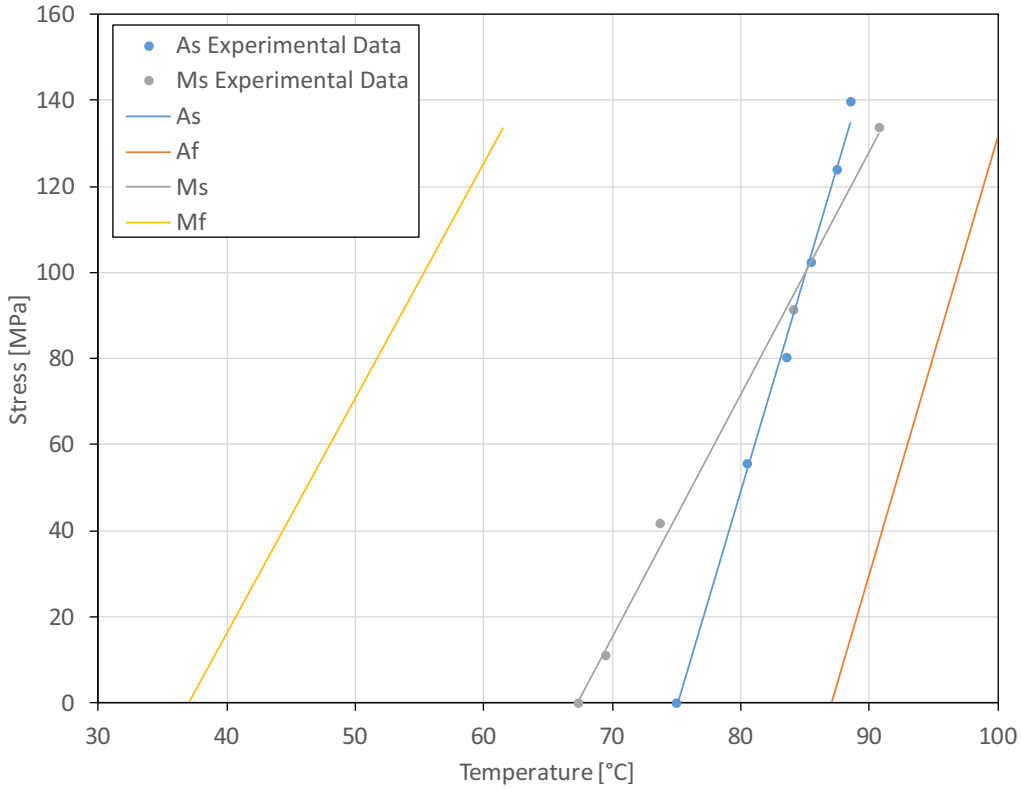

Figure 5.3: Transformation temperatures of austenite and martensite phases of the SME portion of the laser processed SMA actuator verses applied stress. Note the slope of martensite and austenite phase transformations are not the same.

to be parallel respectively. M_s^* and A_s^* are the stress-free transformation temperatures obtained from the DSC results. The experimental data in Figure 5.3 shows the relationships between transformation temperatures and stress. [66]. Note that the the relationship for austenite and martensite are not parallel (Austenite's relationship are steeper than Martensite's) as verified by [67, 68].

Thermal capacity for the PE and SME sections are different. Due to phase transformation SME thermal capacity changes with respect to temperature accounts for the latent

heat of transformation; however, PE does not undergo phase transformation and thus its thermal capacity coefficient is assumed constant. Thermal capacity in the simulation is defined by the following piece-wise relationship:

$$C = \begin{cases} C_{PE} & z \leq L_{PE} \\ C(T)_H & \dot{T} \leq 0 \\ C(T)_C & \dot{T} < 0 \end{cases} \tag{5.5}$$

The stress dependent thermal capacity for the SME portion is modeled based on a normal distribution-like function as shown in Equations 5.6 and 5.7. Where the middle of the curve is the average of phase transformation start and finish temperatures, and standard deviation is 1/6 of the difference of the transformation temperatures which represents 95% of transformation. The result of the thermal capacity model is shown in Figure 5.4.

$$C(T)_H = A_p e^{-18\left(\frac{T-\frac{A_f+A_s}{2}-\frac{\sigma}{C_A}}{A_f-A_s}\right)^2} + Cp \tag{5.6}$$

$$C(T)_C = M_p e^{-18\left(\frac{T-\frac{M_f+M_s}{2}-\frac{\sigma}{C_M}}{M_s-M_f}\right)^2} + Cp \tag{5.7}$$

Since the PE and SME regions have two different material composition, their thermal conductivities are different as well. As a result, thermal conductivity of martensite and austenite is also different, which makes the thermal conductivity of the SME region dependent on its phase transformation. Equation 5.8 describes the thermal conductivity as a weighted series summation of austenite and martensite thermal conductivities. Equation 5.9 is a piece-wise definition of thermal conductivity in the simulation.

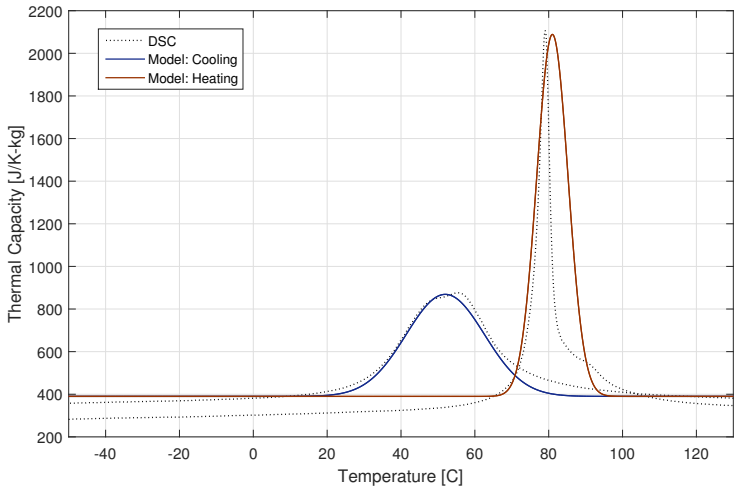

Figure 5.4: Thermal heat capacity obtained from DSC results of the SME portion of the actuator under stress-free conditions as well as the modelled stress-free thermal capacity based on normal distribution function. Note the presence of R-phase in the DSC results and not the Modelled ones.

$$k_{SME}(\xi) = (1-\xi)k_A + \xi k_M \tag{5.8}$$

$$k = \begin{cases} k_{PE} & z \leq L_{PE} \\ k_{SME}(\xi) & otherwise \end{cases} \tag{5.9}$$

For the purposes of simulation, the martensite phase transformation fraction is taken to be the ratio of elongation versus the maximum elongation under a particular stress [64].

The cooling of the actuator wire comes from the heat convection and thermal radiation to the ambient environment. Thermal radiation is neglected and heat convection is implemented as a boundary condition to Equation 5.3. Heat convection coefficient of a cylindrical wire has been studied by [69, 70, 71]. Recently, the effects of angle of the wire

with respect to horizontal on the convection coefficient has been studied by [72] and is show in Equation 5.10.

$$h = \frac{k_\infty}{D}\left[A + C\left(\frac{16g(T - T_\infty)D^3P^2Pr}{\mu^2 T_\infty R_c^2 Z^2 (T + T_\infty)^4}\right)^n\right] \tag{5.10}$$

Where g is gravity constant, R_c is air gas constant, Z is air compressibility factor, D is the diameter of the wire, Pr is the Prandtl number, P is air pressure, μ is air dynamic viscosity, and k is air thermal conductivity. A, B, and n are empirical constants based on the angle of the wire. Since the temperature of the wire is not uniform along its radius and length, the average temperature is considered for the PE and SME sections. The simulation is run multiple times for different applied stresses to the actuator.

5.2.2 SME Modeling & Properties

There are many different approaches to modelling SME behaviour such as micro-mechanical [73, 74] and thermodynamics modelling [67, 75, 76, 77] based on the crystal structure and the fundamental laws of physics. However, they can be very complicated and difficult to define; therefore, a macroscopic phenomenological approach is chosen for the purposes of this study. These types of modelling is very common for the purposes of actuation and controls; and they can be done in two major categories machine learning and numerical methods [78, 79, 80, 11, 20, 81, 22, 82] or mathematical function based. Any of these modelling approaches would work for the proposed actuator design.

Equations 5.11 & 5.12 are a set of logistic functions which phenomenologically model the transformation behaviour by calculating the martensite phase fraction based on empirical results, these specific equations are proposed by Madill et. al [13], and also they are very

Table 5.1: SME Properties

Parameter	Value	Unit
Stress-free Martensite Start (M_S)	67.43	°C
Stress-free Martensite Finnish (M_f)	35.46	°C
Stress-free Austenite Start (A_S)	77.60	°C
Stress-free Austenite Finnish (A_f)	84.56	°C
Austenite Transformation Stress Factor (C_A)	10.091	MPa/°C
Martensite Transformation Stress Factor (C_M)	5.453	MPa/°C
Austenite Peak Thermal Capacity (A_P)	2088.59	J/kg-°C
Martensite Peak Thermal Capacity (M_P)	868.78	J/kg-°C
Base Thermal Capacity (C_P)	390	J/kg-°C
Austenite Thermal Conductivity (k_A)	18	W/m-k
Martensite Thermal Conductivity (k_M)	8.6	W/m-k
Austenite Elastic Modulus (E_A)	75	GPa
Martensite Elastic Modulus (E_M)	28	GPa
Austenite Thermal Expansion (ϑ_A)	11	10^{-6}/°C
Martensite Thermal Expansion (ϑ_M)	6.6	10^{-6}/°C
Initial Length (l_{SME}^0)	200	mm
Diameter (D)	226.06	µm

similar to ones proposed by Jayender et. al.[83]. Verity of other sigmoid-like functions with slightly different curvatures such as cosine and sine [84, 64, 85], error function [61], and inverse tangent have also been used to model SMA phase transformation.

$$M \rightarrow A: \quad \xi(T,\sigma) = \left[\frac{\xi_a}{1+e^{km\left(T-\frac{A_s+A_f}{2}-\frac{\sigma}{Cm}\right)}}\right] + \xi_b \tag{5.11}$$

$$A \rightarrow M: \quad \xi(T,\sigma) = \left[\frac{\xi_a}{1+e^{ka\left(T-\frac{M_s+M_f}{2}-\frac{\sigma}{Ca}\right)}}\right] + \xi_b \tag{5.12}$$

The condition of phase transformation is given by Equations 5.13 & 5.14 as proposed by Elahinia et. al. [64].

$$M \rightarrow A: \quad A_f + \frac{\sigma}{C_A} > T > A_s + \frac{\sigma}{C_A} \quad \& \quad \dot{T} - \frac{\dot{\sigma}}{C_A} > 0 \tag{5.13}$$

$$A \rightarrow M: \quad M_f + \frac{\sigma}{C_M} < T < M_s + \frac{\sigma}{C_M} \quad \& \quad \dot{T} - \frac{\dot{\sigma}}{C_M} < 0 \tag{5.14}$$

Due to the unique and un-optimized material properties, and the presence of R-phase (as evident in Figure 5.4) and other metallurgical phenomena such as a slight two-way shape memory effect of the fabricated actuator, a linear correction to the Equation 5.12 was added to get a better agreement with the experimental results.

Resistance of SME is modeled by the adding the martensite and austenite portions of resistance as set of series resistors with respect to martinsite phase fraction as shown in Equation 5.15. Series summation of austenite and martinsite resistances has also been implemented by [15, 18, 64]. Additionally, since transformation propagation starts from the outer ends of the wire and works its way inwards, there series model makes phenomenological sense as well.

$$R_{SME} = (1 - \xi)R_A + \xi R_M \tag{5.15}$$

The individual resistances of austenite and martensite are modeled as a linear function of stress and temperature, and the correlation is obtained empirically in a set of steady-state experiments previously outlines [86, 15]. Equation 5.16 shows this linear relationship. Constants $R^o_{A,M}$, $R^T_{A,M}$, and $R^\sigma_{A,M}$ are curve fitting parameters and are obtained based on empirical data shown in Figure 4.3.

$$R_{A,M}(\sigma, T) = R^o_{A,M} + R^T_{A,M}T + R^\sigma_{A,M}\sigma \tag{5.16}$$

However, in order to mitigate some of the non-linearity which is exhibited in the resistance behaviour of the Austenite and Martensite [61] the resistance constants are assumed to be different for heating and cooling. These constants are presented in Table 5.2.

Table 5.2: SME Resistance Constants

Parameter	Value		Unit
	Heating	Cooling	
Austenite ER Temp. Constant ($R_A{}^T$)	4.925e-3	4.329e-3	Ω/°C
Martensite ER Temp. Constant ($R_M{}^T$)	0.656e-2	1.049e-2	Ω/°C
Austenite ER Stress Constant ($R_A{}^\sigma$)	4.526e-4	4.548e-4	Ω/MPa
Martensite ER Stress Constant ($R_M{}^\sigma$)	1.383e-3	0.589e-3	Ω/MPa
Austenite ER Constant ($R_A{}^0$)	3.658	3.707	Ω
Martensite ER Constant ($R_M{}^0$)	4.078	4.034	Ω

Similar to Resistance, elastic module of SME is also a function of phase fraction. However, with similar logic as resistance model, the elastic model is added as two elastic members in parallel [87].

$$E_{SME}(\xi) = \frac{1}{\frac{1-\xi}{E_A} + \frac{\xi}{E_B}} \tag{5.17}$$

The classical constitutive model of the SME proposed by Liang et. al. is given as follows [84, 68] and as validated by many of the researchers mentioned such as [65].

$$\dot{\sigma} = E_{SME}(\xi)\dot{\varepsilon}_{SME} + \theta_{SME}(\xi)\dot{T}_{SME} + \Omega(\xi)\dot{\xi} \tag{5.18}$$

θ_{SME} represents the thermal expansion of the and it's also a function of the phase transformation.

$$\theta_{SME} = (1+\xi)\theta_A + \xi\theta_M \tag{5.19}$$

The stress component of the phase transformation Ω is expressed in the Equation 5.20; where, ε_{SME}^{max} is the maximum recoverable strain.

$$\Omega(\xi) = \varepsilon_{SME}^{max} E_{SME}(\xi) \tag{5.20}$$

Table 5.3: PE Properties

Parameter	Value	Unit
Initial Length (l_{PE}^0)	20	mm
Elastic Modulus (E_{PE})	75	GPa
Resistance Constant (R_{PE}^0)	0.3509	Ω
Resistance Stress Constant (R_{PE}^σ)	1.3129E-5	Ω/MPa
Resistance Temperature Constant (R_{PE}^T)	3.8234E-4	Ω/°C
Thermal Expansion (ϑ_{PE})	11	10^{-6}/°C
Thermal Conductivity (k_{PE})	18	W/m-k
Diameter (D)	226.06	µm
Density (ρ)	6450	kg/m^3

The results of the SME modelling under different applied stressed is shown in Figure 5.5 and compared with experimental data. Note that the temperature is simulated and the actual stress on the wire is different than the nominal stress presented on the graph due to fiction of the bearings. The model is much closer to experimental results for the austenite to martensite transformation for material-related reasons mentioned before.

5.2.3 PE Properties & Modeling

Unlike the SME portion of the actuator, the PE portion does not undergo any phase transformation since the applied stress is below the pseudo-elastic plateaus stress as can be seen in Figure 5.2, thus the actuation happens only in the elastic region. Therefore, the maximum stress applied to this actuator design should be below the pseudo-elastic plateau at any given temperature. For this reason, its behaviour is very similar to regular elastic alloys. Thus, the resistance of PE portion's elastic region is linearly dependent on stress and temperature as shown by experimental data in Figure 5.6 and results obtained by Airoldi et. al. [88]. This relationship is presented in Equation 5.21.

$$R_{PE}(\sigma, T) = R_{PE}^o + R_{PE}^T T + R_{PE}^\sigma \sigma \tag{5.21}$$

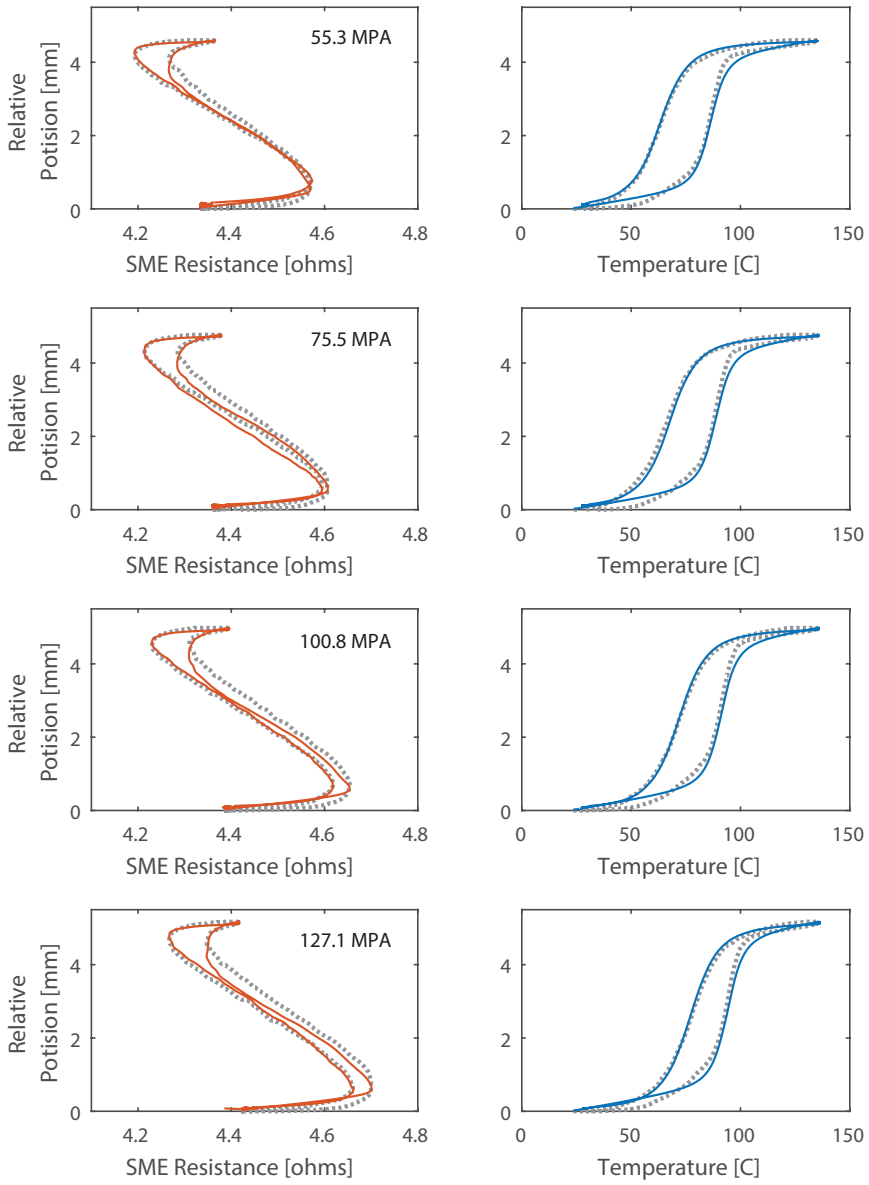

Figure 5.5: Experimental (dotted) and SME model (solid) showing position versus resistance and position versus temperature under different applied stresses.

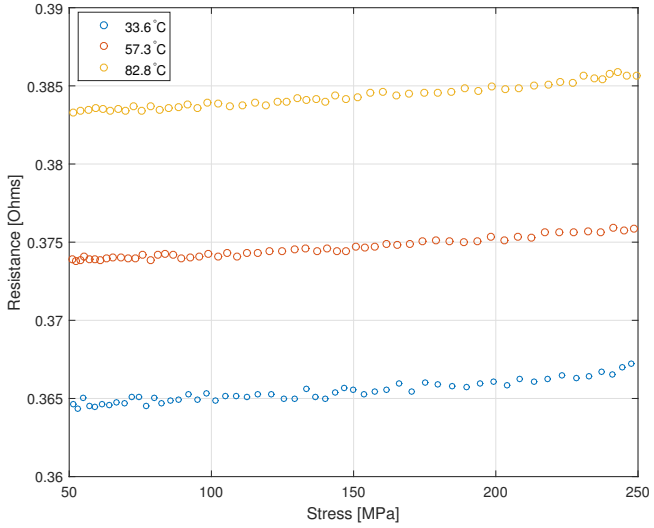

Figure 5.6: Resistance of PE versus different stresses and temperatures.

This linear relationship of PE elasticity can be modeled the same as the SME martensite and austenite resistances expressed in Equation 5.16. Therefore, due to the lack of phase transformation (hysteretic behaviour), an explicit relationship between the temperature of the PE portion and applied stress to the actuator can be obtained. The experimental resistance measurements of the PE region with respect to different stresses and temperatures is shown in Figure 5.6. Due to the lack of phase transformation inf the PE portion of the actuator. It's constitutive model is represented by Equation 5.22.

$$\dot{\sigma} = E_{PE}\dot{\varepsilon}_{PE} + \theta\dot{T}_{PE} \tag{5.22}$$

5.2.4 Controllable Actuation Range

The actuation range of the SMA actuator is dependent on the stress applied to the wire. Only the elongation of the wire that is due to phase transformation and thermal expansion

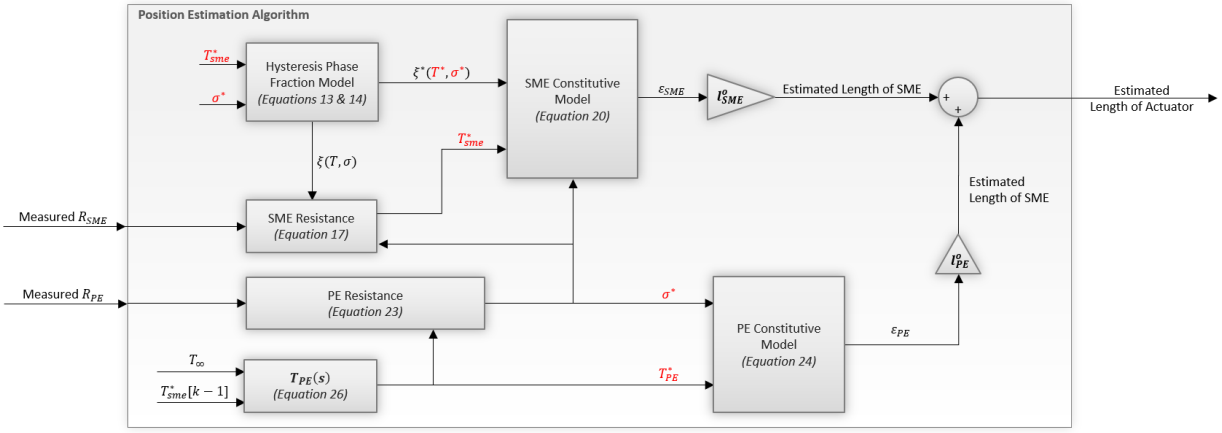

Figure 5.7: Block-diagram showing the conceptual structure of the position, temperature, and stress estimation algorithm.

can be controlled by joules heating and not the elongation caused by elasticity of material. For example, if the SME portion is completely in austenite phase and stress increases, the position of the actuator becomes purely a function of the applied stresses (and negligible thermal expansion) which cannot be controlled by changing the temperature of the wire. Therefore, these limitations of range and stress level have to be thought of for different applications. The overall length of the proposed actuator (actuator position) is expressed in the following Equation 5.23.

$$L = \varepsilon_{PE} L_{PE} + \varepsilon_{SME} L_{SME} \tag{5.23}$$

5.3 Position Estimation Algorithm

Position Estimation Algorithm (PEA) is based on empirical models described in the previous sections. The purpose of this section is to outline an algorithm which estimates the position of the SMA actuator wire by measuring the two Resistances (R_{PE} & R_{SME}) as

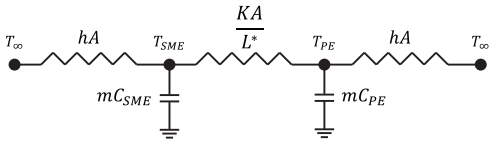

Figure 5.8: Simplified thermal relation ship between the temperature of ambient, SME and PE portions without Joules heating.

proposed earlier. PEA works on the two major assumptions that the PE and SME are both under the same stress and environmental thermal conditions such as ambient temperature and convection.

Since the PE section only operates in its elastic region, there is no phase fraction equation, and the stress-temperature relationship can be directly obtained from Equation 5.21. However, as shown in Figure 5.6, the effects of temperature is much larger than the effects of stress. Therefore, in order to obtain the applied stress, both the temperature and resistance of the PE has to be known. Equation 5.24 is a simplified lumped capacitance thermal transfer function which calculates the temperature of the PE section in real-time and is part of the PEA. It is based on the previous estimated temperature of the SME region, ambient temperature, thermal capacity of PE, resistance of the PE, thermal conductivity, and the electrical current going though the PE region. The distance between the center of the PE portion and SME portion is denoted as L^*. A_{PE} is the surface area of the PE potion. The heat transfer model schematic is illustrated in Figure 5.8.

Since the properties of the PE region are more constant due to the lack of phase transformation, it is easier to calculated the temperature of PE rather than SME on-line.

$$T_{PE}(s) = \frac{I^2 R_{PE} + hA_{PE}T_\infty + \frac{kA_s}{L^*}T_{SME}^{t-1}}{m_{PE}C_{PE}s + \frac{kA_s}{L^*} + hA_{PE}} \tag{5.24}$$

At every time instance, depending on the direction of phase transformation, the Equa-

tions 5.11 or 5.12 are calculated based on the memory-depended constants ξ_a & ξ_b. Then, the calculated martensite phase fraction equation is plugged into the resistance model in Equation 5.15. By measuring the resistance and using Equation 5.15, a relationship between the SME temperature and stress can be obtained for that specific time instance. Thus, by using the stress obtained from the PE region, the temperature of the SME region of the current time can be calculated.

The results could be thought of as estimated temperatures and stress of the actuator wire. These estimated parameters can now be plugged back into both SME and PE models explained in previous sections to obtained a fully solved state of the actuator. Therefore, using the models and the estimated stress and temperatures, the positions (length) of the actuator wire can be estimated under varying applied stresses. Additionally, the estimated stress can be used in any force future control systems. The overall operation of the discussed PEA is summarized in a block diagram illustrate in Figure 5.7.

5.4 Position Estimation Results

In this section the results of the PEA is shown and discussed. Figure 5.9 shows the applied current, estimated and measured position, position error, and measured stress. Initially an open-loop steady state current of 0.34A is supplied to the actuator. Subsequently, the actuator contracts and reaches a steady-state position. At this stage, extra weights are added to increase the applied stress on the actuator wire. As the weights are gradually added, and the wire starts to extend. Finally, a current of 0.6A is supplied to the wire to fully transform it to austenite. As it can be seen from the presented results, the PEA follows the actual position very closely. The maximum position error of 219um is achieved which is approximately 5% of the total actuation under the stress applied.

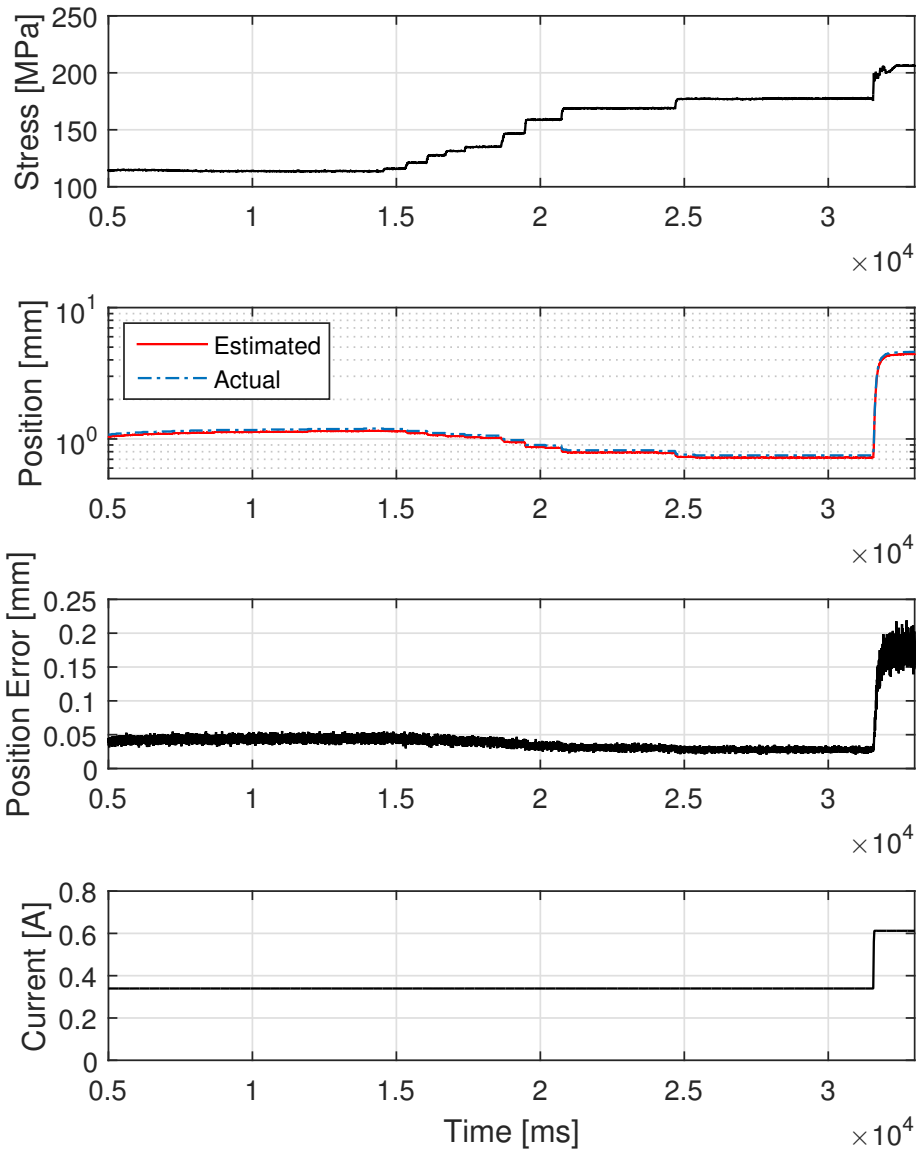

Figure 5.9: Position estimation results showing the estimated position (and position error) under varying stress levels.

The error of PEA increases towards the end of actuation and during the increase in the current. There could be a combination of two explanations for this effect; one reason could be due to the transient behaviour of the PEA during a sudden extra heat is added, the other more likely reason is the difference between the reality and the mathematical model presented specially towards the final portion of the transformation as discussed in previous sections.

Therefore, it's important to notice that this approach relies very heavily on having an accurate empirically based mathematical model for both the PE and SME sections of the wire since, hence any differences between the model and reality will result in an error in the estimated parameters such as position. Parameter identification and adaptive techniques could potentially be used in the future to enhance the material and environmental properties [89].

Thermo-mechanical and micro-structure of this actuator design is not optimized; therefore, some of the presented mathematical models do not match the behaviour of the SMA actuator exactly which is one of the main sources of error in the position estimation. This problem could be mitigated by using machine learning algorithms such as deep neural network DNN to identify the SMA actuator instead of the mathematical models [82]. Additionally, uncertainty about the uniformity of thermal convection along the wire is another source of error.

5.5 Other Dual-Resistance Methods

There are other possibilities of using a dual resistance feedback method for the purposes of controlling a regular SMA actuator. Two possibilities are shown in Figure 5.10. The first possibility consists of placing a stationary prob somewhere in the middle of the wire in a

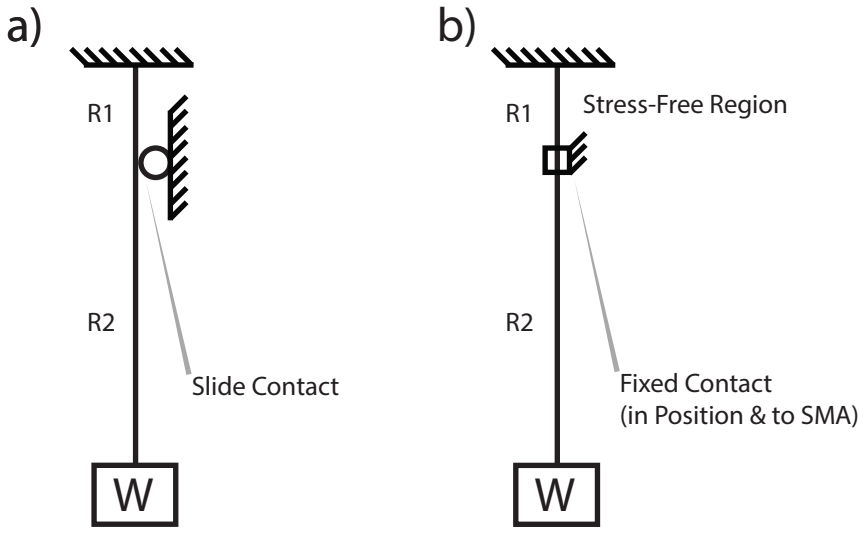

Figure 5.10: Other possible dual-resistance measurement methods: a) using a sliding-contact b) using a stress-reliever fixed contact.

way which the SMA actuator can slid over it. This unique dual-resistance measurement technique is illustrated in Figure 5.10 a) and was first performed by [90, 91, 92]. Since the location of the middle prob is known, it treats the SMA actuator is a kind of voltage divider. Since the electrical resistance of the smaller known distance and the resistance of the larger second section is known; it is assumed that the second section is proportional in length to the known distance given the ratio of the resistances.

The second possibility, however untested, is shown in Figure 5.10 b). The basis of this method is to prevent stress from being transferred to the smaller first section. In this way the two resistances are measured from sections that under go different conditions. The larger section experiences elongation, temperature change, and stress; and the smaller section experiences only temperature change. In this method using some of the equations presented in this section, position and stress of the actuator could be estimated given the assumption that the temperature constant along the length of the wire.

Chapter 6

Novel Position Estimation using High-Frequency Signal Reflection

In this chapter, another novel sensorless position estimation method is proposed, and preliminary experimental results are presented. In the previous Chapters, specifically Chapter 5, sensor-less dual-resistance position (& force) estimation methods were presented. However, in this chapter, a different electrical phenomenon other than resistance is proposed to be used in estimating the position of an SMA actuator. In literature, the only other sensorless method of estimating SMA position is Inductance; however, this method is used mostly on SMA spring actuator due to the significant effect of spring pitch on its inductance [25, 26, 24]. In linear actuators such as SMA wires, measuring the change in inductance is extremely difficult due to the minimal dependency of inductance on the length of the linear wire. But, there are other ways which the laws of nature can be used to amplify a signal which corresponds mainly to the length of the actuator.

6.1 Theory

Waves propagating in many different mediums such as strings and air to name a few. Similar to wave propagation in strings which cause the atoms in the string to follow the wave and move spatial dimensions; electrical signals also propagate through a conductive wire. Once the waves propagating through the string reaches the end, it will reflect back regardless whether the end is kept stationary or free. If the reflected wave has the same amplitude as the original wave, it creates the phenomenon of standing waves. Based on the same analogy, this is the theory behind position estimation using the signal power measurement of the high-frequency standing wave created by the signal reflection at an un-terminated end is shown in Figure 6.1. It's important to notice that the presented method does not require any specially processed SMA and can work on any metallic wires (including SMA actuators). However, since regular metallic wires do not have the same capacity for elongation of an SMA wire, it would not be feasible to measure the length of them using this method. Additionally, this approach is effected minimally by the nonlinear behaviour and hysteresis of the SMA material and is mainly the function of the geometry (length) of the wire. Therefore, this method makes it substantially easier to implement a simple sensor-less control systems. In fact, this phenomenon is regularly seen in high-frequency signal processing and measurements; however, most high-frequency signals are used to transfer information which makes signal reflection and standing waves a parasitic phenomenon. Typically, a variety of steps is taken to eliminate these unwanted reflections in communication signals us as data travelling through coaxial cables for Internet or TV purposes. Therefore, in communication lines, great care is taken into impedance matching of the cables and correct termination for the ends of the connections. The longer the cable, the lower frequency is needed to observe the effect and the reflection.

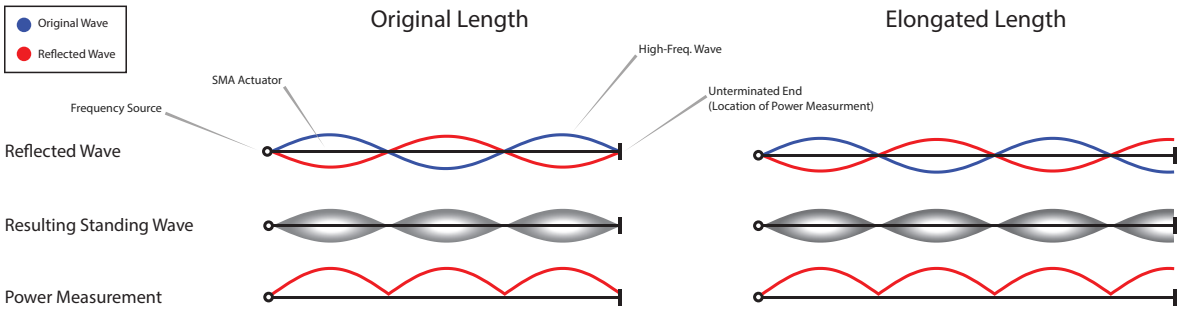

Figure 6.1: Illustration showing position estimation by the high-frequency refection concept.

The speed of the travel of a signal in a conductive wire is measured as a fraction of the speed of light in vacuum, this fraction is known as the "Velocity Factor", and it's calculated as a function of the conductor's relative permittivity κ:

$$VF = \frac{1}{\sqrt{\kappa}} \tag{6.1}$$

This factor could be thought of as speed of sound in a piece of string. Therefore, similarly, the first fundamental frequency in a string is given by:

$$f_1 = \frac{VF \times c}{2L_{wire}} \tag{6.2}$$

Where, C is the speed of light, and L_{wire} is the instantaneous length of the wire. The fundamental frequency is not important for the position estimation because standing waves occur regardless of the signal frequency or speed of wave travel in the conductor as long as the amplitudes of the original and reflected signals are close. Tuning the frequency decides the spatial position of the nodes and anti-nodes along the length of the wire.

For example, for coaxial wires with lengths ranging in the order of meters, reflections of signals with frequencies in the order of MHz can be observed with resealable accuracy.

However, since the length of typical SMA actuators is well below one meter, a much higher frequency is needed to observe more than one wavelength along the length of the wire. Since the waves of this high-frequency signal (both original and reflected) travel very fast at any given physical location along the wire, measuring the transient amplitude of the signal would be hard and not feasible for a cheap sensorless position estimation method. Therefore, the power of the signal at the un-terminated end of the actuator is measured instead of the highly transient amplitude. The following equation describes the standing wave at the end of the wire as a function time:

$$V(t) = V_1 + V_2 = A_1 \sin(\frac{2\pi L_{wire}}{\lambda} - \omega t) + A_2 \sin(\frac{2\pi L_{wire}}{\lambda} + \omega t) \tag{6.3}$$

Assuming that the the reflection amplitude and the original amplitude are the same ($A_1 \approx A_2$), Equation 6.3 simplifies to:

$$V = 2A \sin\left(\frac{2\pi L_{wire}}{\lambda}\right) \cos(\omega t) \tag{6.4}$$

Where the frequency of the signal is f and,

$$\lambda = \frac{VFc}{f} \qquad , and \qquad \omega = 2\pi f \tag{6.5}$$

Typically measuring the signal power is achieved by using commercially available signal power measurement Integrated Circuits (ICs). One can think of this approach as using a natural amplifier to measure the length using high-frequency signals. This approach to estimate the position of the SMA actuator (length) is illustrated in Figure 6.1.

Additionally, the response of the signal power measurement ICs needs to be taken into considerate because of the non-linear frequency and amplitude dependence of these

devices. It's crucial for the signal to be as close to a pure sinusoidal wave as possible. In fact, waves with other shapes, such as square waves, consist of many different frequencies super-positioned as understood from Fourier series fundamentals. This is not to convey that some other similar scheme cannot be implemented by using a square wave.

6.2 Electronic Circuitry

The electronic circuitry of the experiment is relatively simple. It constitutes of a variable frequency generator which is responsible for generating high frequency between 1.6 GHz and 3.0 GHz proportional to the tuning voltage supplied by a Digital to Analogue (DAC) module controlled by PC. It also contains one signal power measurement IC and an Analogue to Digital (ADC) module to convert the measured signal power in forms of a voltage to digital information which is then sent to the PC. The picture of the electronic circuitry is shown in Figure 6.2.

The SMA wire used is a nickel-rich PE wire. SME wire could have been used instead of the PE one; therefore, the nature of the wire does not affect the experiment. For this experiment, based on experimental trials, a signal of 2.45GHz is used as the source for the high-frequency signal. The PE wire is crimped inside two stainless-steel rods. These crimps are held in place inside two plastic (Delrin) pieces for insulation from the rest of electronically conductive setup, and they are primarily responsible for handling the force and not transferring it for the electrical connections. The signals for both the source and power-measurement sides are carried via high-quality 10GHz rated coaxial cables and are connected to the two *SubMiniature version A* connectors which are soldered to the PE wire. The connection configuration is shown in Figure 6.4.

The overall experimental setup is summarized in the schematic shown in Figure 6.3.

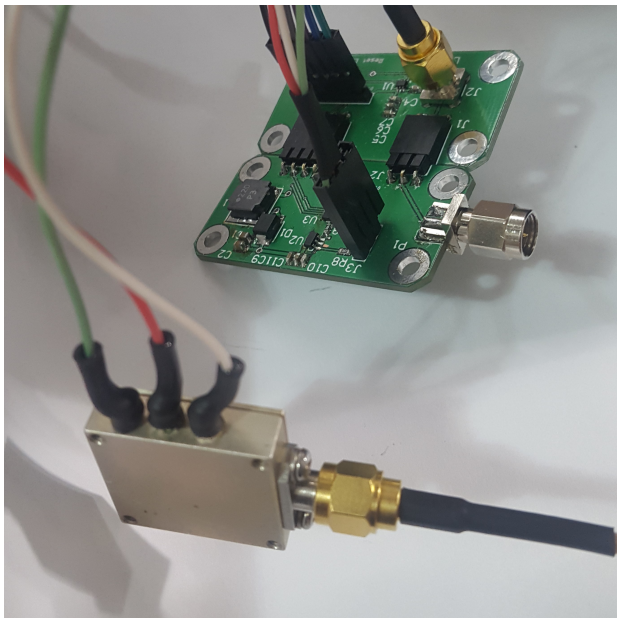

Figure 6.2: Photo of the electronic Circuitry used to supply a tunable high-frequency sinusoidal signal source and the signal power measurement unit.

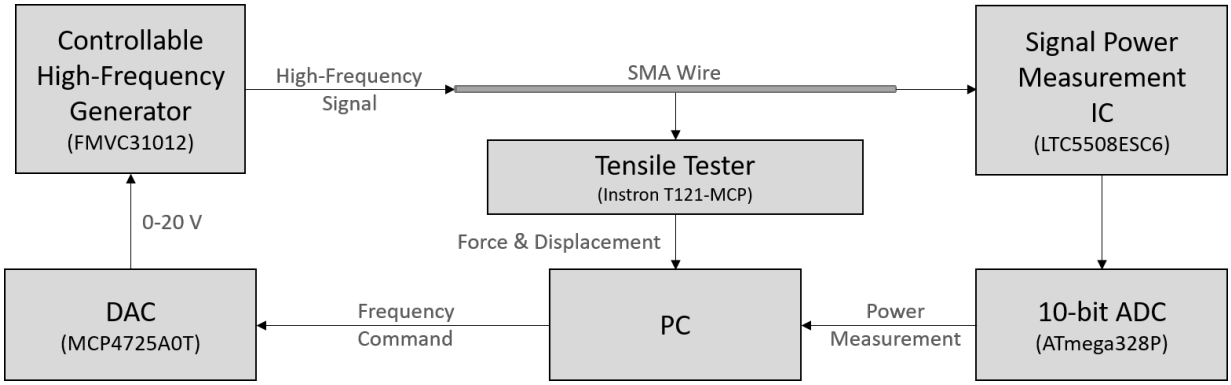

Figure 6.3: Simplified schematic showing the experimental setup used for the high-frequency reflection position estimation concept.

Figure 6.4: The configuration of the connection assembly of the PE SMA wire illustrating the crimping, *SubMiniature version A* connectors, and Delrin insulating block.

6.3 Experimental Setup

The main part of the experimental setup is the industrial tensile tester which is used mostly for metallurgical material characterization. This setup is programmed to tension the wire at a constant strain rate between 0 and 20mm of extension. While the tensile cycling is occurring, a variable frequency generator is supplying single high-frequency signal to one end the SMA wire and signal power measurements are taken at the other un-terminated end. Therefore, at the end of the test extension and force data are gathered by the tensile tester and the signal power measurements and sent to a PC. The photo of the experimental setup is presented in Figure 6.5.

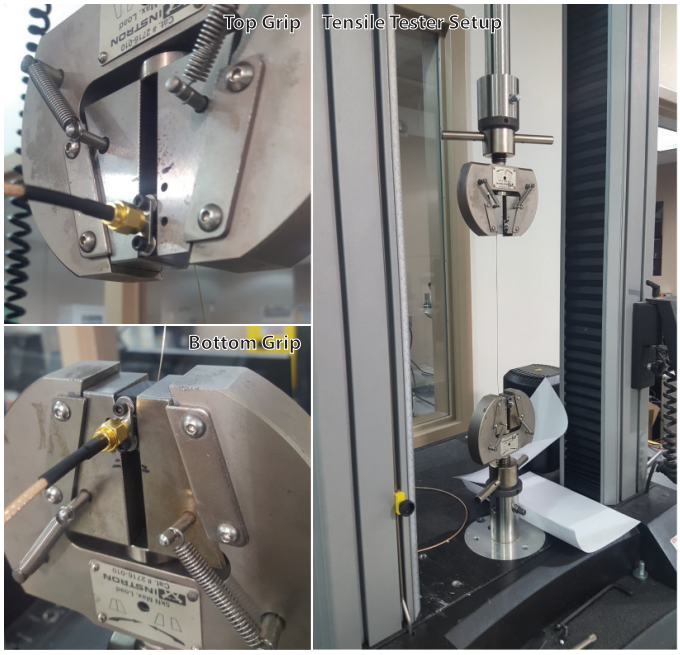

Figure 6.5: Tensile Tester setup showing the mounted PE wire with the two connection assemblies.

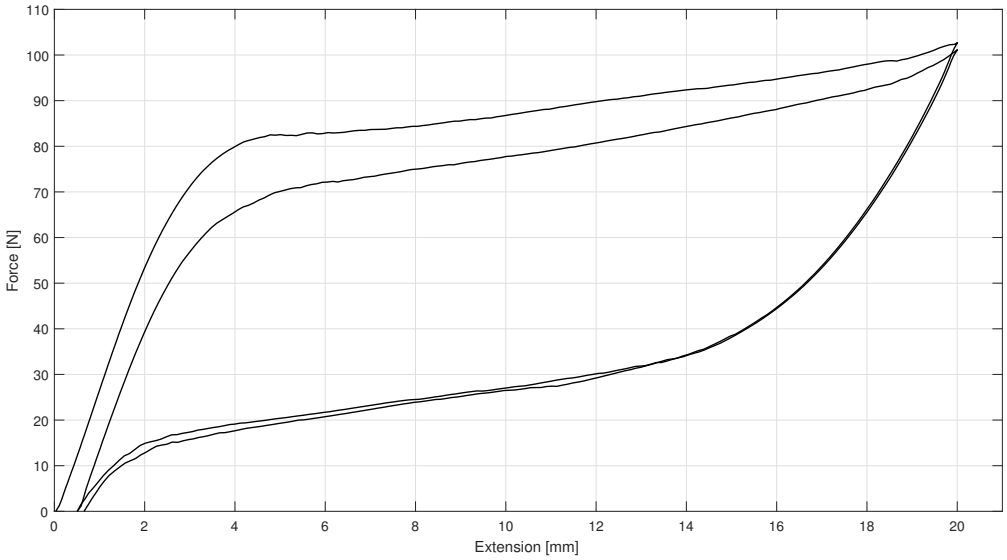

Figure 6.6: Force-Extension of the PE actuator cycled twice to 20mm.

6.4 Experimental Results

In the following section, the measured power of the signal is plotted against the measured position (elongation) of the wire. Since the power and the position measurements are taken from two different equipment, the results were synchronized and interpolated based on time. These results are shown in Figure 6.7. The results show an extremely nice relationship between the measured power and the extension of the wire. As it can be seen by the results and compared to the force-extension results shown in Figure 6.6, even with an untrained SMA wire with substantial mechanical properties from one cycle to another, the power measurements are mostly unaffected. There is, however, a small hysteresis which could be due to the less-than-perfect time synchronization.

In fully-trained SMA actuator, the estimated position using the proposed method in this

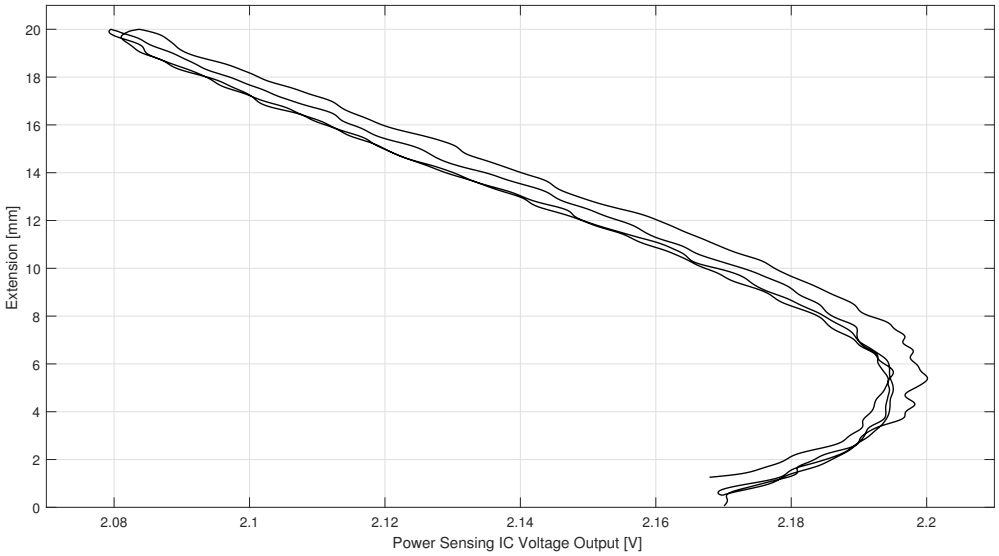

Figure 6.7: Extension data obtained from the tensile tester versus time.

chapter can be utilized along with equations presented in previous chapters to estimate the force acting on the actuator wire. The primary challenge of this approach is Joule's heating using a low-frequency source and sensing using a high-frequency source concurrently using a single electronic board. This is the next crucial step to achieve a fully closed feedback loop using this method.

Chapter 7

Simple Position & Force Control

In this chapter, a simple position control scheme of the novel SMA actuator with self-sensing dual resistance feedback is discussed, and it's position tracking results are presented. It's important to notice that the control scheme is implemented on an actuator wire which is slightly different than the one used in previous chapters. This is due to the lack of mass production capability and quality management of the product of the wires are not guaranteed and slight variations exit.

Previously, in the literature, there have been many control schemes implemented using both self-sense resistance feedback or direct position sensor feedback. For example, in [93] a tangential sliding mode controller with a time delay estimation is used for precision position tracking with a position sensor feedback. In this paper the results were compared to a simple PID control system, and the results showed a significant improvements specially on faster position tracking. In [16], a simple PID controller with feed-forward inverse compensator controls the position of a spring-biased SMA actuator using resistance feedback. Additionally, [8] compared two modified PID controllers with forward compensates with a regulate PID controller using position sensor feedback signal. Therefore, PID controller is a good first choice for position control of the proposed SMA actuator with dual-resistance.

7.1 Position & Force Control Schemes

For proof of concept purposes of controlling the proposed actuator using the dual-resistance self-sense method described in Chapter 5, only a simple PID controller is used even-though it does not provide the best transient response because of the non-linear behaviour of the SMA with hysteresis. Figure 7.1 illustrates the simple position controller. The controller has the following PID values: $K_p = 80$, $K_i = 15$, and $K_d = 8$. These values are not optimized and were obtained using trial and error basis. Additionally, a software saturation block is added to the output of the PID to ensure the current remains between a maximum 1A and a minimum 0.1mA. The current cannot be zero since the feedback signals are based on resistances of the wire. It's important to know that the experimental setup is the same as described earlier in Chapter 4.

Since there is noise present in the resistance measurement signals, the corresponding estimated position (or force) also carries a proportional and compounded noise of both SME and PE resistance as shown in Figure 5.9 Chapter 5. Therefore, a low-pass filter with a cut-off frequency of 100Hz is used to improve the performance of the controller. The average controller response performance of all the different step commands are summarized in Table 7.1. It's important to note that since the material exhibits non-linear behaviour it's, the controller performance does not strictly follow a linear time-invariant systems.

7.1.1 Force Control Results

In this section, the force control results are shown. In this experiment both the top and bottom of the actuator is constrained which means the actuator cannot contract upon heating which results in an increase in the applied reaction forces. The results are shown in Figure 7.2. In this experiment four step force commands are issued by the controller

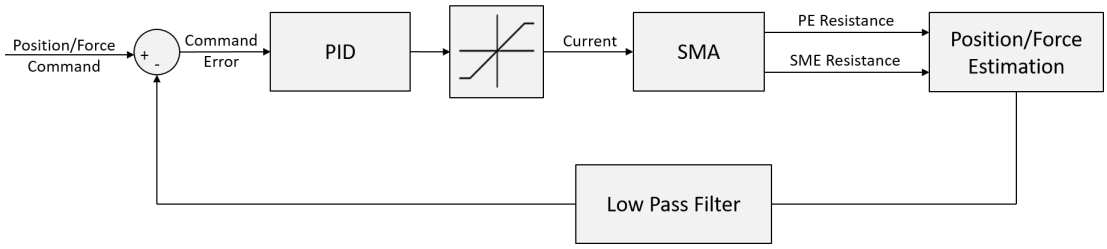

Figure 7.1: Simple PID position control scheme using the position/force estimated feedback based on the dual-resistance.

and the controller varies the current output to the SMA wire to achieve the commanded forces based on the two PE and SME resistances. The average performance of the force controller is summarized in Table 7.1.

Based on the obtained results, the controller achieves reasonable force tracking on the heating, how ever on the cooling the controller has a relatively large overshoot due to hysteresis. The force controller has an average RMS error of 30.72[g] and an average rise time of 2.87[s] which is about three times faster than the position controller. Also, the average settling time for the force controller is about twice faster than the position controller.

7.1.2 Position Control Results

In this section, two position control results are presented. In these experiment the top of the actuator is constrained but the bottom of the actuator is constrained which means the actuator is free to move upon heating. The first experiment is a series of step position command which the controller tries to achieve. The results of the first experiment is shown in Figure 7.3. In the second experiment, the position tracking performance of the control scheme under unknown time varying loads is tested by changing the load mid-way through the experiment. The results are shown in Figure 7.4. The average performances of the

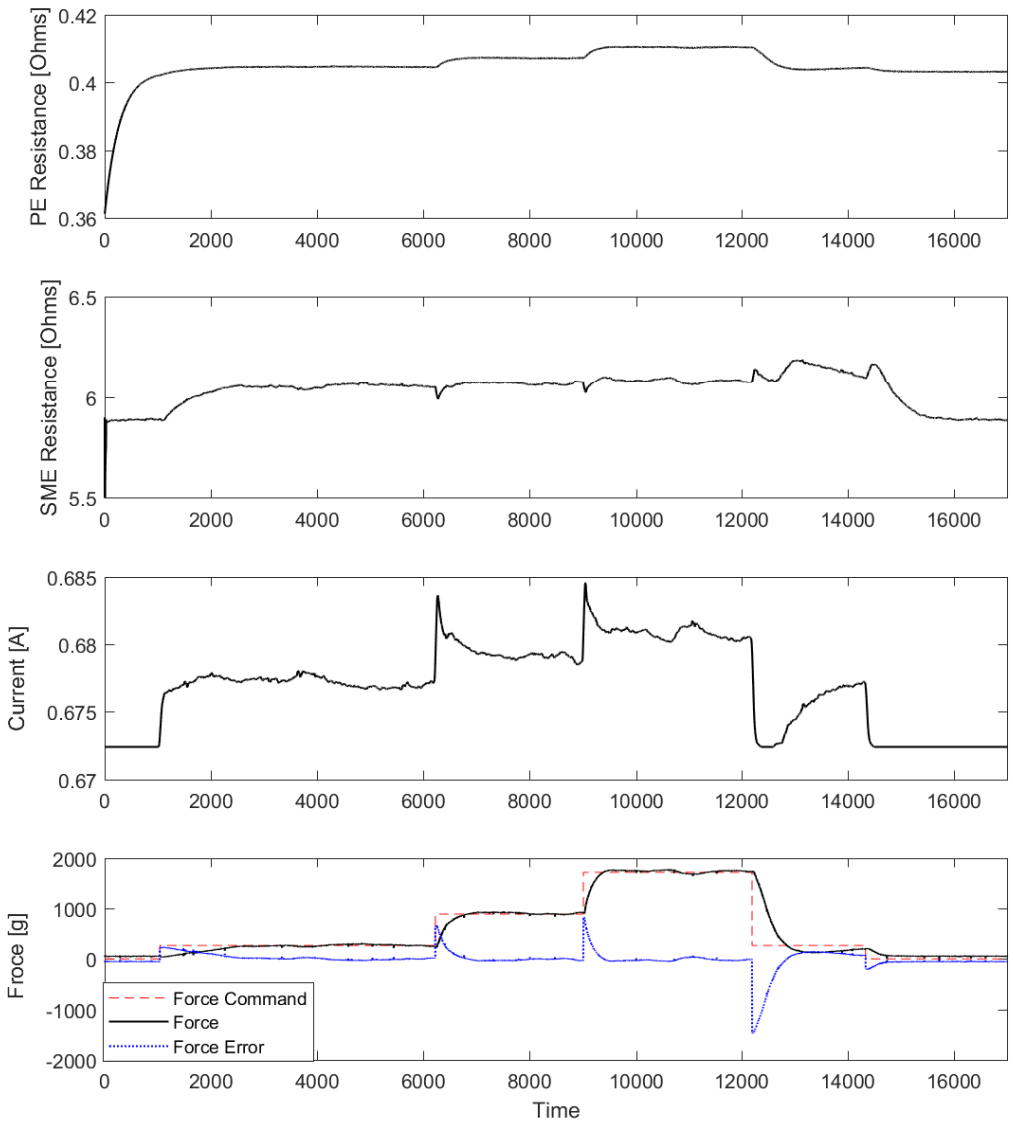

Figure 7.2: Force control response to step force command. Force commanded, actual force, force error, PE resistance, SME resistance, and current are presented for the simple PID controller.

position controller is summarized in Table 7.1.

Table 7.1: Force & Position Controller Average Performance

	Average SS RMS Error	Average Rise Time	Average Settling Time
Force Control	30.72 [g]	2.87 [s]	6.32 [s]
Position Control	0.27 [mm]	8.97 [s]	12.75 [s]

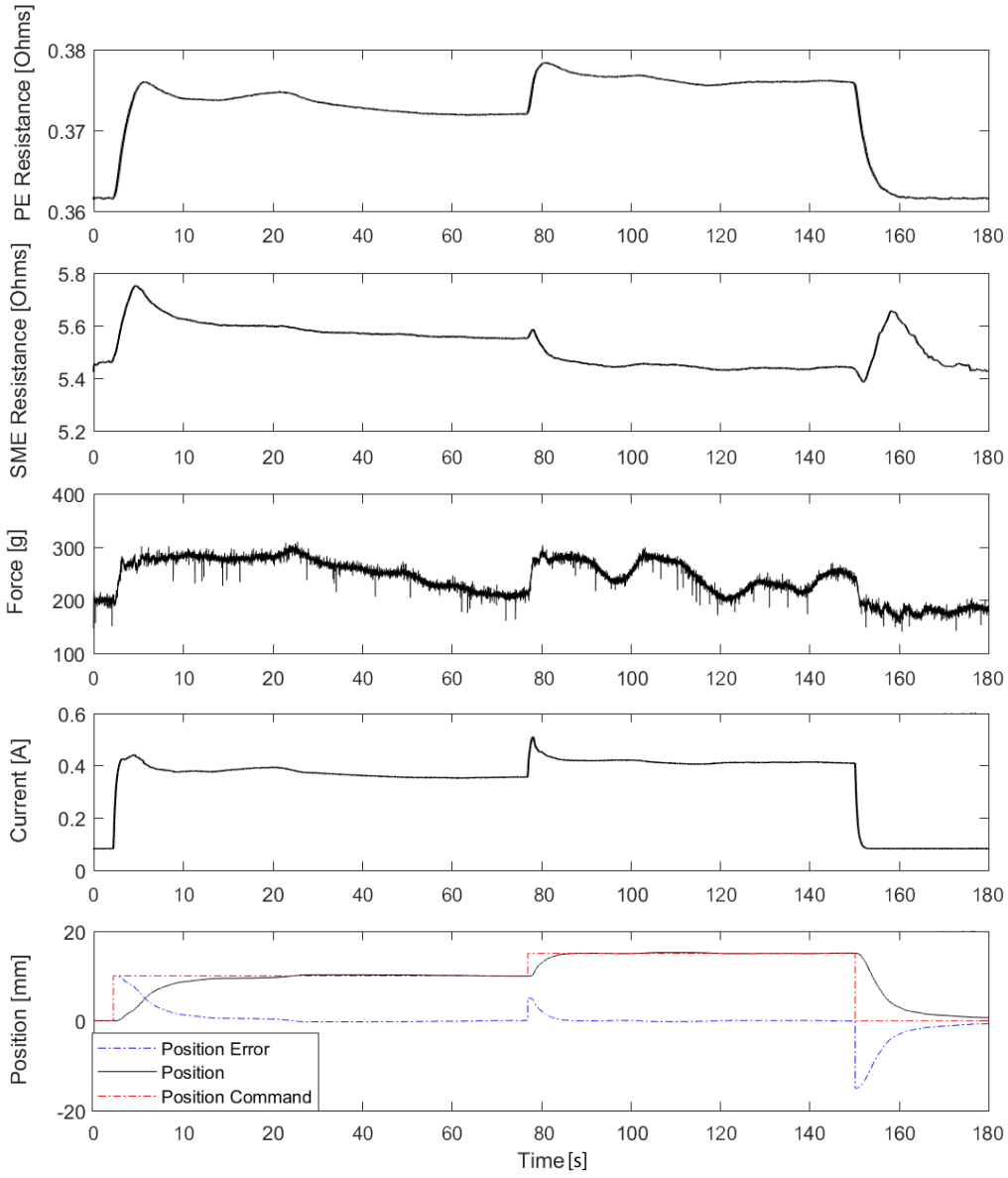

Figure 7.3: Position control response to step position command. Position commanded, actual position, position error, force, PE resistance, SME resistance, and current are presented for the simple PID controller.

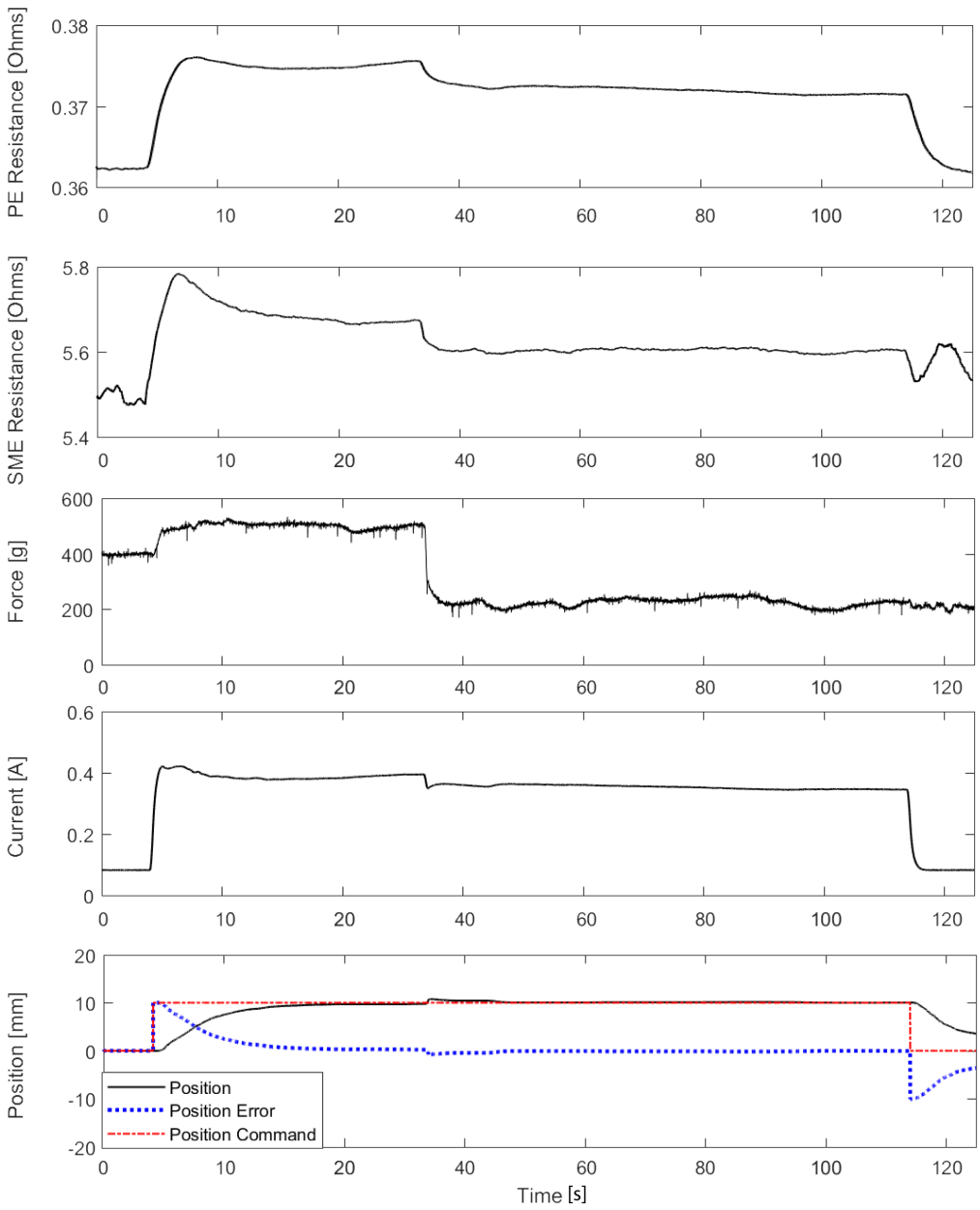

Figure 7.4: Regulating position under changing load. Position commanded, actual position, position error, force, PE resistance, SME resistance, and current are presented for the simple PID controller.

Chapter 8

Conclusion & Future Works

In this chapter major achievements of the thesis and the outlook towards the future works are discussed.

8.1 Conclusion

1. A novel laser processed NiTi SMA actuator design with an embedded strain gauge sensor containing two different material compositions in one monolithic piece of actuator wire is proposed, and its fabrication process was discussed in detail in Section 5.1. The actuator was fabricated using the designed automated wire-feeding laser system described in Chapter 3.

2. The effects of laser pulse power and pulse time on NiTi phase transformation temperatures of Nickel-rich NiTi SMA wire are examined in Section 3.2. It is shown for the first time that the exact temperatures of the phase transformation could be fine-tuned precisely by changing the laser pulse power and pulse time. Previously this was achieved by changing the pulse overlap or number of pulses per spot.

3. An electronic circuit board is designed as described in Section 4.1 to be a linear current source power supply for the actuator as well as measure high-side resistances very accurately. This electronic board is also responsible for calculating the control algorithm in real-time as well.

4. A model-based position estimation algorithm is developed based on the proposed actuator design. The algorithm uses the two measured resistances to estimate the force and position of the actuator as described in detail in Chapter 5. The position estimation could achieve a 95% accuracy. ss

5. Subsequently, the proposed model was used in a simple PID position (and force) control system as a proof of concept. The results showed that even with an un-optimized control system the position and the force could be controlled with reasonable accuracy. The results of theses experiments are presented in Chapter 7.

6. Another novel high-frequency reflection sensorless position estimation method with preliminary results are presented in Chapter 6. These results show that the position can be correlated accurately to the power measurement of a high-frequency reflected signal even though the material has non-linear and unstable properties with very large hysteresis.

8.2 Contributions

8.2.1 Refereed Journal Publications:

1. Zamani, N., Khamesee, M. B., & Khan, M. I. (2017). *Novel Laser Processed Shape Memory Alloy Actuator Design with an Embedded Strain Gauge Sensor using Dual Resis-*

tance Measurements. Part I: Fabrication and Model-Based Position Estimation. Sensors and Actuators A: Physical.

8.2.2 Refereed Conference Proceedings:

1. Zamani, N., Khamesee, M. B. (2016). *Temperature Control of NiTi Shape Memory Alloy (SMA) using Adaptively Identified Thermal Convective Coefficient.* ASME Annual Conference on Information Storage & Processing Systems (ISPS).

2. Zamani, N., Khamesee, M. B., & Khan, M. I. (2017). *Novel Monolithic Shape Memory Alloy (SMA) Actuator with an Embedded Strain Gauge Sensor.* The International Conference on Shape Memory and Superelastic Technologies (SMST).

8.2.3 Patents:

1. Laser Processed Shape Memory Alloy Actuator Design with an Embedded Strain Gauge Sensor. Part I: Fabrication and Model Based Position Estimation. N. Zamani, M. I. Khan, assignee. Patent K8001665.

8.3 Future Works

The field of MMM-processed SMA is fascinating and filled with possibilities in the ever growing world of actuation. In this final section of the thesis, some of the potential future works are outlined.

One of the first steps that need to be taken is to improve and streamline the material properties and fabrication process to create a more suitable material properties for the proposed actuator design. For example, a material which does not contain an R-phase

would substantially improve the position estimation accuracy of the novel actuator deign. The effects of laser processing on the properties of SMA is not well understood; therefore, there is a need for multi-physics simulations and models that predict laser-induced nickel-evaporation process and validate it with the experimental results shown in Chapter 3. Similar multi-physics simulations and models of key-hole laser processing have been performed before [94, 95, 96, 97, 98], These studies could be used as the basis and modified for this specific application. Moreover, other methods such as machine learning should be investigated to control the position (or force) of the actuator under time-varying applied loads [20, 99, 81, 22]. This could potentially eliminate the problem of needing to create a complex mathematical model to predict the behaviour of SMAs.

One of the most significant advantages of MMM-process is the ability to incorporate self-biasing into SMA actuators [100]. Moreover, the combination of self-biasing and self-sensing should be further studied. For example by using the MMM technology a monolithic linear-spring combined actuator could be fabricated and which would provide self-biasing using the Spring portion and self-sensing using electrical resistance and inductance measurements. Other actuation geometries are also of great interest such as sheet actuators which has a potential of being an entirely separate and indented category of MMM-processes actuation.

Moreover, other sensorless position (or force) estimation methods such as the one presented in Chapter 6 should be further investigated. The high-frequency reflection position estimation method should be incorporated into a control system to better understand the advantages, disadvantage, and overall industrial feasibility of such approach. It's important to comprehend that sensor-less control of SMA actuators is crucial to the successes and viability of the technology in competition with other actuation technologies in real-world applications. Due to some inherent shortcomings of SMAs such as relatively slow

cooling, the scope of the feasibility of using SMAs is very narrow; therefore in the industry, sensor-less control of SMA actuators might be the difference between success and failure.

The other major limitation of the SMA actuators, slow cooling rate, should be addressed as well. This could be accomplished by two means: passive (or active) cooling of SMA actuators, and(or) by using HTSMAs. For both of these two means steps could be taken to improve the performance. For example, for passive cooling, the effective surface area could be increased by using a thermal heat sink in conjunction with a non-toxic liquid metal such as Gallium as a thermally conductive medium between SMA and the heat sink. Additive laser processing techniques could be used to create localized HTSMA by alloying ternary elements into the alloys as mentioned in Chapter 1 Section 2.1.2. Using both the subtractive (MMM-process) and additive laser processes in combination could potentially revolutionize the field of SMA actuation due to the vast possibilities it provides.

Even though a simple position and force control system was presented in Chapter 7, there are many better performing and comprehensive control schemes which could be implemented along with the dual-resistance sensorless position estimation scheme to control the novel proposed SMA actuator with an embedded strain gauge. Sliding-Mode Controller (SMC) is one of the examples of such control schemes which is an improvement on a simple PID controller [17, 101, 93, 90, 12].

References

[1] A. Ölander, "An electrochemical investigatio of solid cadmium-gold alloys," *Journal of American Chemical Society*, vol. 54, no. 1906, pp. 3819–3833, 1932.

[2] Y. Luo, T. Takagi, S. Maruyama, and M. Yamada, "A Shape Memory Alloy Actuator Using Peltier Modules and R-Phase Transition," *Journal of Intelligent Materials Systems and Structures*, vol. 11, no. 7, pp. 503–511, 2000.

[3] K. D. Laurentis, A. Fisch, J. Nikitczuk, and C. Mavroidis, "Optimal design of shape memory alloy wire bundle actuators," *Proceedings 2002 IEEE International Conference on Robotics and Automation (Cat. No.02CH37292)*, vol. 3, no. May, pp. 2363–2368, 2002.

[4] K. T. O'Toole, M. M. McGrath, and E. Coyle, "Analysis and evaluation of the dynamic performance of SMA actuators for prosthetic hand design," *Journal of Materials Engineering and Performance*, vol. 18, no. 5-6, pp. 781–786, 2009.

[5] M. J. Mosley and C. Mavroidis, "Design and Control of a Shape Memory Alloy Wire Bundle Actuator," *DETC'00: 26th Biennial Mechanisms and Robotics Conference*, vol. 123, no. March 2001, pp. 1–7, 2000.

[6] J. Frenzel, A. Wieczorek, I. Opahle, B. Maa??, R. Drautz, and G. Eggeler, "On the effect of alloy composition on martensite start temperatures and latent heats in Ni-Ti-based shape memory alloys," *Acta Materialia*, vol. 90, pp. 213–231, 2015.

[7] S. M. Saghaian, H. E. Karaca, H. Tobe, J. Pons, R. Santamarta, Y. I. Chumlyakov, and R. D. Noebe, "Effects of Ni content on the shape memory properties and microstructure of Ni-rich NiTi-20Hf alloys," *Smart Materials and Structures*, vol. 25, no. 9, p. 095029, 2016.

[8] Á. Villoslada, N. Escudero, F. Martín, A. Flores, C. Rivera, M. Collado, and L. Moreno, "Sensors and Actuators A : Physical Position control of a shape memory alloy actuator using a four-term bilinear PID controller," vol. 236, pp. 257–272, 2015.

[9] S. Hattori, M. Hara, H. Nabae, D. Hwang, and T. Higuchi, "Design of an impact drive actuator using a shape memory alloy wire," *Sensors and Actuators, A: Physical*, vol. 219, pp. 47–57, 2014.

[10] Z. Guo, Y. Pan, L. B. Wee, and H. Yu, "Design and control of a novel compliant differential shape memory alloy actuator," *Sensors and Actuators, A: Physical*, vol. 225, pp. 71–80, 2015.

[11] H. Sayyaadi and M. R. Zakerzadeh, "Position control of shape memory alloy actuator based on the generalized Prandtl-Ishlinskii inverse model," *Mechatronics*, vol. 22, no. 7, pp. 945–957, 2012.

[12] J. C. Hannen, J. H. Crews, and G. D. Buckner, "Indirect intelligent sliding mode control of a shape memory alloy actuated flexible beam using hysteretic recurrent neural networks," *Smart Materials and Structures*, vol. 21, no. 8, p. 085015, 2012.

[13] D. R. Madill and D. Wang, "Modeling and L2-Stability of a Shape Memory Alloy Position Control System," *TRANSACTIONS ON CONTROL SYSTEMS TECHNOLOGY*, vol. 6, no. 4, pp. 473–481, 1998.

[14] K. Ikuta, "SHAPE MEMORY ALLOY SERVO ACTUATOR SYSTEM WITH ELECTRIC RESISTANCE FEEDBACK AND APPLICATION FOR ACTIVE ENDOSCOPE Koji," *IEEE*, pp. 427–430, 1988.

[15] R. Yousefian, M. a. Kia, and M. H. Zadeh, "Sensorless resistive-based control of shape memory alloy actuators in locking mechanism," *Journal of Intelligent Material Systems and Structures*, vol. 26, pp. 450–462, apr 2014.

[16] S.-H. Liu, T.-S. Huang, and J.-Y. Yen, "Tracking Control of Shape-Memory-Alloy Actuators Based on Self-Sensing Feedback and Inverse Hysteresis Compensation," *Sensors*, vol. 10, no. 1, pp. 112–127, 2009.

[17] G. Song, V. Chaudhry, and C. Batur, "Precision tracking control of shape memory alloy actuators using neural networks and a sliding-mode based robust controller," *Smart Materials and Structures*, vol. 12, pp. 223–231, apr 2003.

[18] H. Song, E. Kubica, and R. Gorbet, "RESISTANCE MODELLING OF SMA WIRE ACTUATORS," No. November, 2011.

[19] N. T. Tai and K. K. Ahn, "A hysteresis functional link artificial neural network for identification and model predictive control of SMA actuator," *Journal of Process Control*, vol. 22, no. 4, pp. 766–777, 2012.

[20] H. Wang and G. Song, "Innovative NARX recurrent neural network model for ultra-thin shape memory alloy wire," *Neurocomputing*, vol. 134, pp. 289–295, 2014.

[21] D. Josephine Selvarani Ruth, S. Sunjai Nakshatharan, and D. Dhanalakshmi, "Differential resistance feedback control of a self-sensing shape memory alloy actuated system," *ISA Transactions*, vol. 53, no. 2, pp. 289–297, 2014.

[22] N. Ma, G. Song, and H.-J. Lee, "Position control of shape memory alloy actuators with internal electrical resistance feedback using neural networks," *Smart Materials and Structures*, vol. 13, pp. 777–783, aug 2004.

[23] T.-M. Wang, Z.-Y. Shi, D. Liu, C. Ma, and Z.-H. Zhang, "An accurately controlled antagonistic shape memory alloy actuator with self-sensing.," *Sensors (Basel, Switzerland)*, vol. 12, pp. 7682–700, jan 2012.

[24] M. Sreekanth and A. T. Mathew, "Rise time based characterization of sub-millimeter SMA helical actuator for sensorless displacement estimation," pp. 343–347, 2015.

[25] H. Kim, Y. Han, D. young Lee, J.-I. Ha, and K.-J. Cho, "Sensorless displacement estimation of a shape memory alloy coil spring actuator using inductance," *Smart Materials and Structures*, vol. 22, no. 2, pp. 025001—-, 2013.

[26] J. V. D. Weijde, E. Vlasblom, P. Dobbe, H. Vallery, and M. Fritschi, "Force Sensing for Compliant Actuators Using Coil Spring Inductance," no. 1, pp. 2692–2697, 2015.

[27] M. I. Khan, *Pulse Nd:YAG Laser Processing of Nitinol*. PhD thesis, University of Waterloo, 2011.

[28] A. Pequegnat, *Novel Laser Based NiTi Shape Memory Alloy Processing Protocol for Medical Device Applications By*. PhD thesis, 2014.

[29] M. H. Elahinia, M. Hashemi, M. Tabesh, and S. B. Bhaduri, "Manufacturing and processing of NiTi implants: A review," *Progress in Materials Science*, vol. 57, no. 5, pp. 911–946, 2012.

[30] T. B. Massalski, H. Okamoto, P. R. Subramanian and L. Kacprzak, "Binary Alloy Phase Diagrams," *ASM International*, 1990.

[31] D. C. Lagoudas, *Shape Memory Alloys. Springer.* 2008.

[32] O. F. Gerb, "SHAPE MEMORY DEVICE HAVING TWO-WAY CYCLICAL SHAPE MEMORY EFFECT DUE TO COMPOSITIONAL GRADIENT AND METHOD OF MANUFACTURE," 2004.

[33] F. Auricchio and V. Massarotti, "One Way and Two Way Shape Memory Effect : Thermo Mechanical Characterization of Ni Ti wires," p. 92, 2008.

[34] C.-Y. Chang, D. Vokoun, and C.-T. Hu, "Two-way shape memory effect of NiTi alloy induced by constraint aging treatment at room temperature," *Metallurgical and Materials Transactions A*, vol. 32, no. 7, pp. 1629–1634, 2001.

[35] K. Atli, I. Karaman, R. Noebe, and D. Gaydosh, "The effect of training on two-way shape memory effect of binary NiTi and NiTi based ternary high temperature shape memory alloys," *Materials Science and Engineering: A*, vol. 560, pp. 653–666, 2013.

[36] K. C. Atli, I. Karaman, R. D. Noebe, G. Bigelow, and D. Gaydosh, "Work production using the two-way shape memory effect in NiTi and a Ni-rich NiTiHf high-temperature shape memory alloy," *Smart Materials and Structures*, vol. 24, no. 12, p. 125023, 2015.

[37] L. Contardo and G. Guénin, "The Two Way Memory Effect in a Cu-Zn-Al Alloy: The Behaviour during the Training Process," *Materials Science Forum*, vol. 56-58, no. 7, pp. 529–534, 1990.

[38] C. Urbina, S. De La Flor, F. Gispert-Guirado, and F. Ferrando, "New understanding of the influence of the pre-training phase transformation behaviour on the TWSME in NiTi SMA wires," *Proceedings of the Society for Experimental Mechanics, Inc.*, vol. 53, no. 6, pp. 1415–1436, 2013.

[39] J. Wang, *Multiple Memory Material Processing for Augmentation of Local Pseudoelasticity and Corrosion Resistance of NiTi-based Shape Memory Alloys*. PhD thesis, University of Waterloo, 2013.

[40] S. K. Bhaumik, K. V. Ramaiah, and C. N. Saikrishna, "NickelTitanium shape memory alloy wires for thermal actuators," *in Micro and Smart Devices and Systems*, pp. 181–198, 2014.

[41] L. Fumagalli, F. Butera, and A. Coda, "SmartFlex® NiTi Wires for Shape Memory Actuators," *Journal of Materials Engineering and Performance*, vol. 18, no. 5-6, pp. 691–695, 2009.

[42] T. W. Duerig, K. N. Melton, and D. Stöckel, *Engineering Aspects of Shape Memory Alloys*. 1990.

[43] W. Tang, "Thermodynamic study of the low-temperature phase B19 and the martensitic transformation in near-equiatomic Ti-Ni shape memory alloys," *Metallurgical and Materials Transactions A*, vol. 28, no. 3, pp. 537–544, 1997.

[44] M. I. Khan, A. Pequegnat, and Y. N. Zhou, "Multiple memory shape memory alloys," *Advanced Engineering Materials*, vol. 15, no. 5, pp. 386–393, 2013.

[45] B. Panton, *Laser Processing, Thermomechanical Processing, and Thermomechanical Fatigue of NiTi Shape Memory Alloys*. PhD thesis, University of Waterloo, 2016.

[46] M. Daly, *Thermomechanical response of laser processed nickel-titanium shape memory alloy*. PhD thesis, University of Waterloo, 2012.

[47] M. K. A Pequegnat, MDaly, JWang, Y Zhou, "Dynamic actuation of a novel laser-processed NiTi linear actuator," *IOPscience*, 2012.

[48] J. Frenzel, E. P. George, A. Dlouhy, C. Somsen, M. F. X. Wagner, and G. Eggeler, "Influence of Ni on martensitic phase transformations in NiTi shape memory alloys," *Acta Materialia*, vol. 58, no. 9, pp. 3444–3458, 2010.

[49] Y. Liu and P. G. McCormick, "Thermodynamic analysis of the martensitic transformation in NiTi-I. Effect of heat treatment on transformation behaviour," *Acta Metallurgica Et Materialia*, vol. 42, no. 7, pp. 2401–2406, 1994.

[50] G. Tadayyon, S. M. Zebarjad, Y. Guo, M. Mazinani, S. A. Tofail, and M. J. Biggs, "The effect of annealing on the mechanical properties and microstructural evolution of Ti-rich NiTi shape memory alloy," *Materials Science and Engineering: A*, vol. 662, pp. 564–577, 2016.

[51] F. B. Fernandes, K. Mahesh, and A. d. S. Paula, "Thermomechanical treatments for Ni-Ti alloys," *Shape Memory Alloys: Processing, Characterization and Applications Processing, Characterization and Applications*, pp. 3–26, 2013.

[52] D. Chrobak, D. Stróz, and H. Morawiec, "Effect of early stages of precipitation and recovery on the multi-step transformation in deformed and annealed near-equiatomic NiTi alloy," *Scripta Materialia*, vol. 48, no. 5, pp. 571–576, 2003.

[53] M. Karimzadeh, M. R. Aboutalebi, M. T. Salehi, S. M. Abbasi, and M. Morakabati, "Adjustment of Aging Temperature for Reaching Superelasticity in Highly Ni-rich Ti-51.5Ni NiTi Shape Memory Alloy," *Materials and Manufacturing Processes*, vol. 6914, no. June 2015, p. 150603134932001, 2015.

[54] J. Khalil-Allafi, G. Eggeler, a. Dlouhy, W. W. Schmahl, and C. Somsen, "On the influence of heterogeneous precipitation on martensitic transformations in a Ni-rich NiTi shape memory alloy," *Materials Science and Engineering A*, vol. 378, no. 1-2 SPEC. ISS., pp. 148–151, 2004.

[55] K. Wada and Y. Liu, "Thermomechanical training and the shape recovery characteristics of NiTi alloys," *Materials Science and Engineering A*, vol. 481-482, no. 1-2 C, pp. 166–169, 2008.

[56] R. Lahoz and J. a. Puértolas, "Training and two-way shape memory in NiTi alloys: Influence on thermal parameters," *Journal of Alloys and Compounds*, vol. 381, no. 1-2, pp. 130–136, 2004.

[57] D. Converter and T. A. Note, "AVR121: Enhancing ADC resolution by oversampling Microcontrollers," pp. 1–48, 2005.

[58] Atmel, "8-bit AVR Microcontrollers, Aplication Note," p. 15, 2006.

[59] F. P. Incropera, D. P. DeWitt, T. L. Bergman, and A. S. Lavine, *Fundamentals of Heat and Mass Transfer*, vol. 6th of *Dekker Mechanical Engineering*. Wiley, 7th ed., 2007.

[60] S. G. Shu, D. C. Lagoudas, D. Hughes, and J. T. Wen, "Modeling of a flexible beam actuated by shape memory alloy wires," *Smart Mater. Struct.*, vol. 265, pp. 265–277, 1997.

[61] S. M. Dutta and F. H. Ghorbel, "Differential Hysteresis Modeling of a Shape Memory Alloy Wire Actuator," *ASME TRANSACTIONS ON MECHATRONICS*, vol. 10, no. 2, pp. 189–197, 2005.

[62] M. H. Elahinia and H. Ashrafiuon, "Nonlinear Control of a Shape Memory Alloy Actuated Manipulator," *Jour. of Vibration and Acoustics*, vol. 124, no. 4, p. 566, 2002.

[63] J. J. Zhang, Y. H. Yin, and J. Y. Zhu, "Electrical resistivity-based study of self-sensing properties for shape memory alloy-actuated artificial muscle.," *Sensors (Basel, Switzerland)*, vol. 13, no. 10, pp. 12958–12974, 2013.

[64] M. H. Elahinia and M. Ahmadian, "An enhanced SMA phenomenological model: I. The shortcomings of the existing models," *Smart Materials and Structures*, vol. 14, no. 6, pp. 1297–1308, 2005.

[65] M. H. Elahinia and M. Ahmadian, "An enhanced SMA phenomenological model: II. The experimental study," *Smart Materials and Structures*, vol. 14, no. 6, pp. 1297–1308, 2005.

[66] M. Frost, P. Sedlák, M. Sippola, and P. Šittner, "Thermomechanical model for NiTi shape memory wires," *Smart Materials and Structures*, vol. 19, no. 9, p. 094010, 2010.

[67] M. a. Qidwai and D. C. Lagoudas, "Numerical implementation of a shape memory alloy thermomechanical constitutive model using return mapping algorithms," *International Journal for Numerical Methods in Engineering*, vol. 47, no. 6, pp. 1123–1168, 2000.

[68] L. C. Brinson, "Dimensional Constitutive Behavior of Shape Memory Alloys: Thermomechanical Derivation With Non-Constant Material Functions and Redefined Martensite Internal Variable," *Journal of intelligent material systems and structures*, vol. 4, no. 2, pp. 229–242, 1993.

[69] K. Universiq, "Natural Convection Heat Transfer From a Vertical," pp. 1–10, 1999.

[70] S. K. S. Boetcher, "Natural Convection from Circular Cylinders," *Springer*, 2014.

[71] S. M. Dutta, F. H. Ghorbel, and J. B. Dabney, "Modeling and Control of a Shape Memory Alloy Actuator," pp. 1007–1012, 2005.

[72] A. Eisakhani, R. Gorbet, and J. R. Culham, "Electrical Resistance and Natural Convection Heat Transfer Modeling of Shape Memory Alloy Wires," *Proceedings of the ASME 2014 International Mechanical Engineering Congress and Exposition*, pp. 1–10, 2014.

[73] M. Huang, X. Gao, and L. C. Brinson, "Multivariant micromechanical model for SMAs. Part 2. Polycrystal model," *International journal of plasticity*, vol. 16, no. 10, pp. 1371–1390, 2000.

[74] X. Gao, M. Huang, and L. C. Brinson, "Multivariant micromechanical model for SMAs. Part 1. Crystallographic issues for single crystal model," *International journal of plasticity*, vol. 16, no. 10, pp. 1345–1369, 2000.

[75] J. A. Shaw, "A thermochemical model for a 1-D shape memory alloy wire with propagating instabilities," *International Journal of Solids and Structures*, vol. 39, no. 5, pp. 1275–1305, 2002.

[76] J. Boyd and D. Lagoudas, "A thermodynamical constitutive model for shape memory materials. Part I. The monolithic shape memory alloy," *International Journal of Plasticity*, vol. 12, no. 6, pp. 805–842, 1996.

[77] J. A. Shaw, B.-c. Chang, M. A. Iadicola, and Y. M. Leroy, "Thermodynamics of a 1 D shape memory alloy : modeling , experiments , and application,"

[78] G. V. Webb and D. C. Lagoudas, "Hysteresis Modeling of SMA Actuators for Control Applications," 1990.

[79] R. Gorbet, D. Wang, and K. Morris, "Preisach model identification of a two-wire SMA actuator," *Proceedings. 1998 IEEE International Conference on Robotics and Automation (Cat. No.98CH36146)*, vol. 3, no. May, pp. 2161–2167, 1998.

[80] H. Luo, Y. Liao, E. Abel, Z. Wang, and X. Liu, "Hysteresis behavious and modeling of SMA actuators," *Shape Memory Alloys*, pp. 61–80, 2010.

[81] a.a. Adly and S. Abd-El-Hafiz, "Using neural networks in the identification of Preisach-type\nhysteresis models," *IEEE Transactions on Magnetics*, vol. 34, no. 3, pp. 629–635, 1998.

[82] L. Chuntao and T. Yonghong, "A neural networks model for hysteresis nonlinearity," *Sensors and Actuators, A: Physical*, vol. 112, no. 1, pp. 49–54, 2004.

[83] J. Jayender, R. Patel, S. Nikumb, and M. Ostojic, "Modeling and Control of Shape Memory Alloy Actuators," *IEEE Transactions on Control Systems Technology*, vol. 16, pp. 279–287, mar 2008.

[84] C. Liang and C. a. Rogers, "Design of Shape Memory Alloy Actuators," *Journal of Intelligent Material Systems and Structures*, vol. 8, no. 4, pp. 303–313, 1997.

[85] E. Ayvali and J. P. Desai, "Pulse width modulation-based temperature tracking for feedback control of a shape memory alloy actuator.," *Journal of intelligent material systems and structures*, vol. 25, pp. 720–730, apr 2014.

[86] V. Novák, P. Šittner, G. Dayananda, F. Braz-Fernandes, and K. Mahesh, "Electric resistance variation of NiTi shape memory alloy wires in thermomechanical tests: Experiments and simulation," *Materials Science and Engineering: A*, vol. 481-482, pp. 127–133, may 2008.

[87] C. Maletta, E. Sgambitterra, F. Furgiuele, R. Casati, and A. Tuissi, "Fatigue of pseudoelastic NiTi within the stress-induced transformation regime: a modified Coffin-Manson approach," *Smart Materials and Structures*, vol. 21, no. 11, p. 112001, 2012.

[88] G. Airoldi, D. a. Lodi, and M. Pozzi, "The Electric Resistance of Shape Memory Alloys in the Pseudoelastic Regime," *Le Journal de Physique IV*, vol. 07, no. C5, pp. C5–507–C5–512, 1997.

[89] P. Ioannou and B. Fidan, *Adaptive Control Tutorial*. Society for Industrial and Applied Mathematics.

[90] R. N. Saunders, J. G. Boyd, D. J. Hartl, M. A. Savi, P. M. C. L. Pacheco, M. S. Garcia, T. R. Lambert, A. Gurley, and D. Beale, "SMA actuator material model with self- sensing and sliding-mode control ; experiment and multibody dynamics model,"

[91] A. Gurley and R. Broughton, "SMASIS2016-9242," pp. 1–7, 2016.

[92] A. Gurley, W. D. Beale, R. Broughton, and R. Lambert, "Robust Self-Sensing in NiTi Actuators Using a Dual Measurement Technique Objective Why Focus on SMA ?,"

[93] J. Lee, M. Jin, and K. K. Ahn, "Precise tracking control of shape memory alloy actuator systems using hyperbolic tangential sliding mode control with time delay estimation," *Mechatronics*, vol. 23, no. 3, pp. 310–317, 2013.

[94] M. et. al Courtois, "Keyhole Formation During Spot Laser Welding: Heat and Fluid Flow Modeling in a 2D Axisymmetric Configuration," *COMSOL Conference*, no. Figure 2, pp. 1–6, 2012.

[95] M. Courtois, M. Carin, P. Le Masson, S. Gaied, and M. Balabane, "A complete model of keyhole and melt pool dynamics to analyze instabilities and collapse during laser welding," *Journal of Laser Applications*, vol. 26, no. 4, p. 042001, 2014.

[96] M. Courtois, M. Carin, P. Le Masson, S. Gaied, and M. Balabane, "A complete heat and fluid flow modeling of keyhole formation and collapse during spot laser welding," *Icaleo 2013*, p. 1, 2013.

[97] V. Bruyere, C. Touvrey, and P. Namy, "Comparison between Phase Field and ALE Methods to model the Keyhole Digging during Spot Laser Welding," pp. 1–7, 2013.

[98] I. Tomashchuk, I. Bendaoud, P. Sallamand, E. Cicala, S. Lafaye, and M. Almuneau, "Multiphysical modelling of keyhole formation during dissimilar laser welding," no. 3, 2016.

[99] N. Nikdel, P. Nikdel, M. A. Badamchizadeh, and I. Hassanzadeh, "Using neural network model predictive control for controlling shape memory alloy-based manipulator," *IEEE Transactions on Industrial Electronics*, vol. 61, no. 3, pp. 1394–1401, 2014.

[100] A. Pequegnat, B. Panton, Y. N. Zhou, and M. I. Khan, "Local composition and microstructure control for multiple pseudoelastic plateau and hybrid self-biasing shape memory alloys," *Materials & Design*, vol. 92, pp. 802–813, 2016.

[101] Y. Shtessel, C. Edwards, L. Fridman, and A. Levant, *Sliding Mode Control and Observation*. 2014.

APPENDICES

Appendix A

Software and GUI

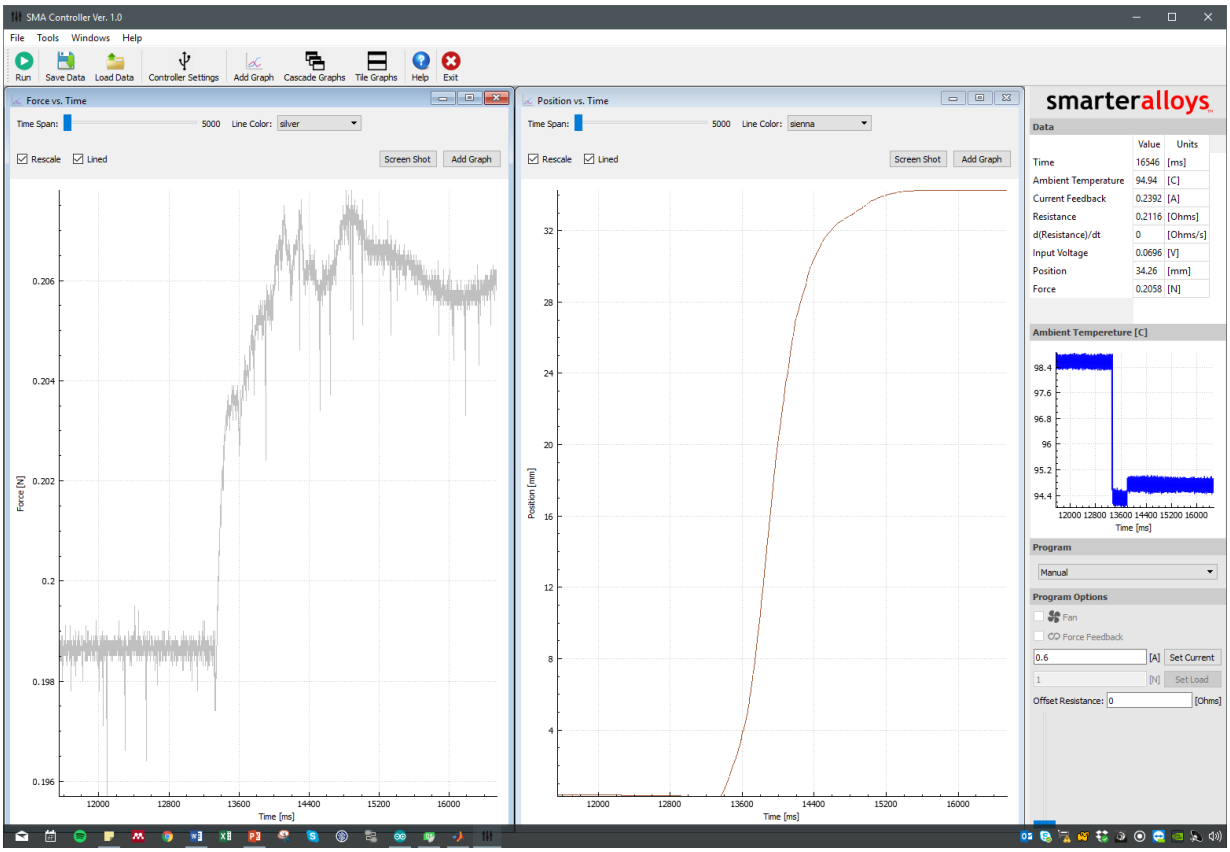

Figure A.1: Screen-shot photo of the software showing the visualization and logging of the measured data.

Appendix B

Setup Photos

Figure B.1: Photo of control setup.

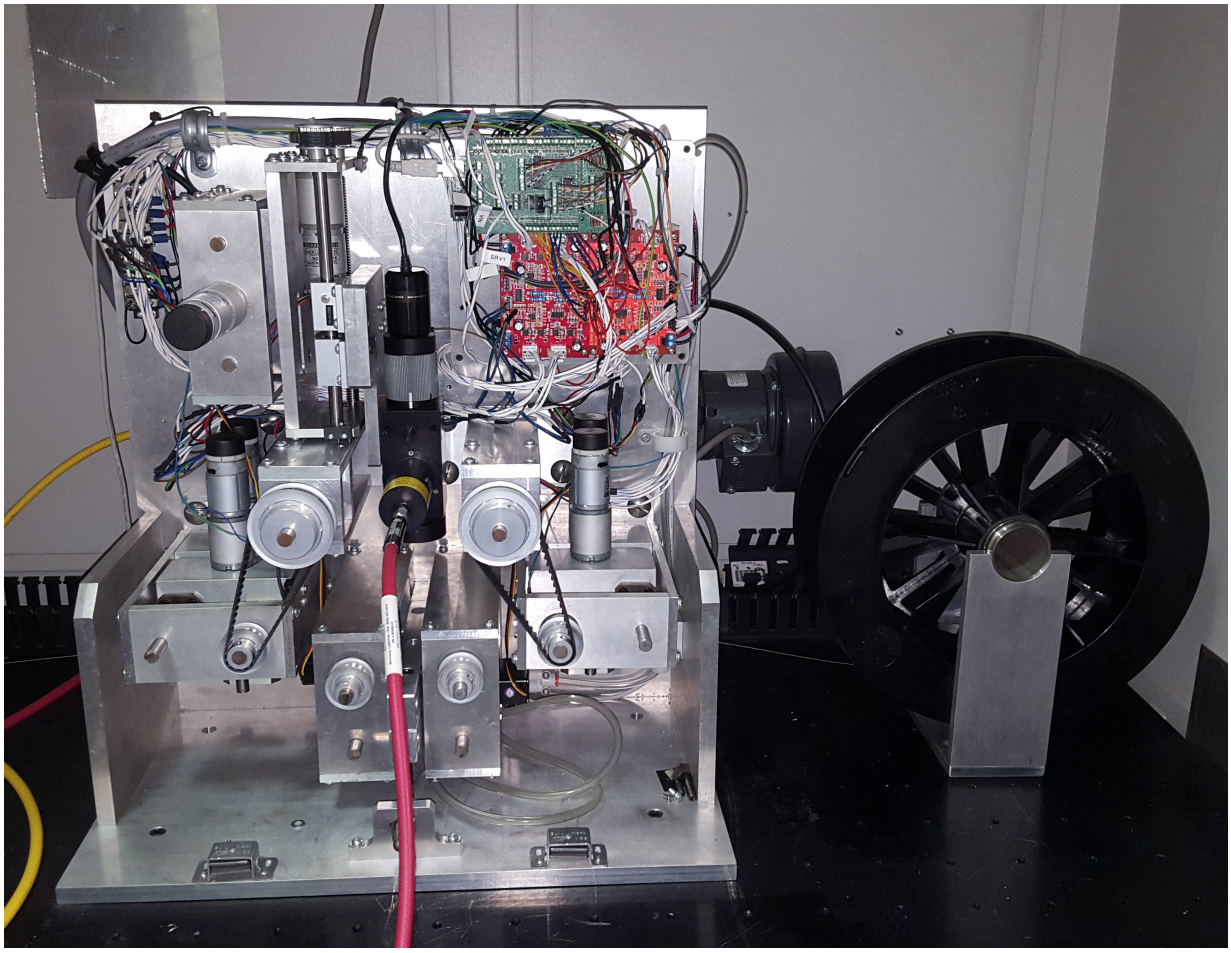

Figure B.2: Photo of wire feeding and laser processing SMA fabrication setup.